On the Role of Fracture Systems in Groundwater-Driven Alpine Slope Deformation

N. Oestreicher[1*], Q. Lei[1], S. Loew[1], C. Roques[1,2]

[1]Department of Earth Sciences, ETH Zürich, Switzerland
[2]CHYN, Université de Neuchâtel

Key Points:

- Migrating pore pressure plumes control the recharge-related subsurface strain field and temporally varying surface displacement vectors
- Significant deformations are expected to occur only in a narrow permeability range, typically observed in fractured crystalline rocks
- Our model explains field observations of surface displacement's magnitude, orientation and hysteresis in the Aletsch valley, Switzerland

*

Corresponding author: N. Oestreicher, Nicolas.Oestreicher@erdw.ethz.ch

Abstract

We study the physical mechanisms that drive alpine slope deformation during water infiltration and depletion into fractured bedrocks. We develop a fully coupled hydromechanical model at the valley scale with multiscale fracture systems ranging from meter to kilometer scales represented. The model parameterized with realistic rock mass properties captures the effects of fractures via an upscaling framework with equivalent hydraulic and mechanical properties assigned to local rock mass blocks. The important heterogeneous and anisotropic characteristics of bedrocks due to depth-dependent variations of fracture density and stress state are taken into account and found to play a critical role in groundwater recharge and valley-scale deformation. Our simulation results show that pore pressure actively diffuses downward from the groundwater table during a recharge event, rendering a critical hydraulic response zone controlling surface deformation patterns. During the recession, the hydraulic front migrates downwards and the deformation recorded at the surface (up to ∼4 cm) rotates accordingly. The most essential parameters in our model are the fracture network geometry, initial fracture aperture (controlling the rock mass permeability), and regional stress conditions. The magnitude and orientation of our model's transient annual slope surface deformation are consistent with field observations at our study site in the Aletsch valley. Our research findings have important implications for understanding groundwater flow and slope deformations in alpine mountain environments.

Plain Language Summary

Groundwater recharge in alpine valleys mainly occurs during snowmelt and sometimes during rainstorm events. When recharge builds up groundwater pressure in the fractured rock mass, the rock mass deforms, which causes complex displacement patterns at the slope surface. Here, we model this coupled process at the scale of an alpine valley with up to millions of fractures to investigate how the fracture system and regional stress condition affect the surface deformation magnitude and orientation. We show that the deformation is constrained by a deep pressurized zone below the valley ridges, which we call the hydraulic response zone (HRZ). The shape and location of the HRZ change throughout the year and control the complex patterns of hysteretic surface displacements. We compare our modeling results with our long-term deformation records from the lower Aletsch Valley and show that we can reproduce and explain the field observations. This

work brings a better understanding of the fracture networks' role in surface deformations induced by recharge-related pore pressure variations. It suggests that the surface deformation patterns may also be used to infer information about the location and depth of the HRZ.

1 Introduction

The central European Alps uplift at rates over 2 mm/y as shown by recent geodetic studies (Sternai et al., 2019; Sánchez et al., 2018). On top of this secular trend, some mountain slopes are subject to strong, often centimetric, seasonal deformations (Hansmann et al., 2012; Glueer et al., 2021; Oestreicher et al., 2021). These annual cyclic deformations could induce progressive rock mass fatigue (Eberhardt et al., 2016), contribute to long-term rock mass damage and participate in the initiation of slope instabilities (Grämiger et al., 2020). In some cases, they may also cause cracking of sensitive infrastructures such as concrete arch dams (Hansmann et al., 2012). Several studies have shown that these ground deformations are caused by natural seasonal variations of recharge and groundwater levels in phreatic mountain aquifers (e.g. Loew et al., 2007; Hansmann et al., 2012; Rouyet et al., 2017; Serpelloni et al., 2018; Silverii et al., 2020; Pintori et al., 2021; Oestreicher et al., 2021). While pore pressure changes associated with groundwater recharge in aquifers drive rock mass deformation (one-way coupling, e.g., Loew et al., 2015; Preisig et al., 2012), stress/strain changes in solid skeletons could also, in turn, cause pore pressure variations and affect groundwater flow in geological formations (Biot, 1941; Terzaghi, 1923; H. F. Wang, 2000; Manga et al., 2012; Min et al., 2004). Due to the heterogeneous nature of alpine mountain slopes, the detailed understanding of the underlying physical mechanisms of such cyclic slope deformations in alpine valleys and their spatio-temporal dynamics remains challenging.

Rock slopes in alpine regions are commonly characterized by natural fracture systems (e.g. joints and faults) across many different length scales (Bonnet et al., 2001; Lei & Wang, 2016). These discontinuities in rock often exhibit a wide range of fracture lengths that may follow a power-law distribution (Bonnet et al., 2001; Lei & Wang, 2016). They tend to play a crucial role in coupled hydromechanical processes in geological media (Rutqvist & Stephansson, 2003; Lei et al., 2017), often serving as the main pathways for groundwater flow (Banks & Robins, 2002; Pruess, 1999; Liu et al., 2002; Lei et al., 2020) and dominating the mechanical properties of rock masses (Hoek & Brown, 1997; Einstein et al., 1983; Eberhardt et al., 2004; Lei & Gao, 2018). An increased pore pressure may lead to a reduction of the effective stress on fracture walls, causing fracture opening and shear reactivation (Zimmerman & Main, 2004; Lei & Barton, 2022). In turn, the normal opening and shear dilation of a fracture would lead to an increase of fracture aperture and permeability (Lei et al., 2016, 2015; Witherspoon et al., 1980; Bandis et al., 1983; Barton et al., 1985). Numerous studies have investigated the two-way hydromechanical coupling in the context of fluid injection and hydraulic stimulation (e.g. Salimzadeh et al., 2018; Dutler et al., 2020; Lei et al., 2021) as well as underground excavations (e.g. Zhao et al., 2021; Tsang et al., 2012), but limited research has been done regarding natural groundwater fluctuations and related slope deformations in alpine mountains. Some studies of one-way coupling have been done, however, without considering discrete fractures and the stress effect on groundwater flow (Grämiger et al., 2020).

At the scale of an alpine valley slope, the groundwater flow is strongly influenced by the topography (Gleeson & Manning, 2008; Welch & Allen, 2012; Goderniaux et al., 2013) and the bedrock permeability structure which is often characterized by a high-permeability zone at shallow depth (Manning & Ingebritsen, 1999; Achtziger-Zupančič et al., 2017; Welch & Allen, 2014; Rapp et al., 2020; Fu et al., 2022). Moon et al. (2020) show that stress conditions in the subsurface, influencing the normal closure and shear dilation of fractures, explain the zone of high permeability in the near-surface (in the first few hundreds of meters). In addition, as shown in many places, the fracture density is also depth dependent with a high fracture density in the near-surface promoting an enhanced permeability as well (e.g. Moon et al., 2020). It is yet unclear what consequences such large permeability gradients in the near subsurface have on the pore pressure-related surface deformation magnitude and orientation.

While the annual recharge and recession-related surface deformation magnitudes in alpine valleys have been addressed in several papers, no detailed investigations of the underlying processes and resulting displacement patterns have been carried out so far. In this paper, we investigate the effects of fractures on the spatial and seasonal rock mass deformation patterns (displacement vector magnitudes, annual hysteresis and vector orientations) associated with transient groundwater flow through bedrock slopes. We develop a fully coupled hydromechanical model simulating the essential processes and phenomena within kilometric height valley flanks with the multiscale fracture system represented. We focus on Alpine recharge cycles, with dominant groundwater recharge from snowmelt in late spring to early summer and groundwater depletion during the rest of the year. We investigate the role of the depth-dependent fracture density, the role of main fracture network properties, and the role of the regional stress conditions on valley surface deformations. This paper is organized as follows. In Section 2, we discuss some key observations of groundwater-related slope deformation signals in our study area, the Aletsch valley in Switzerland, and introduce the fracture pattern and geology at the study site. The conceptual model presented in this paper is driven by these observations and integrates realistic parameter ranges for this type of fractured bedrock alpine valley. In Section 3, we present the mathematical formulations of the fully coupled hydromechanical model followed by the model setup shown in Section 4. The Section on simulation results (Section 5) describes in detail how subsurface coupled processes control surface displacement patterns. This includes the temporal and spatial variations of pore pressure and rock mass deformations during recharge events and subsequent groundwater depletion periods, and the effects of selected key parameters, such as fracture orientation, density, aperture and regional stress field. We finally discuss the results in a broader hydrogeological context and compare them with the surface deformations observed in the Aletsch valley (Section 6).

2 Groundwater-Related Deformation in the Aletsch Valley

Ground surface displacements have been monitored around the tongue of the Great Aletsch Glacier (Southern Swiss Alps) by Glueer et al. (2021) and Oestreicher et al. (2021) since 2012, using continuous Global Positioning System (cGPS) stations (Limpach et al., 2016). The six cGPS stations (i.e., AL01, AL02, AL03, ALTS, ALTD, and FIES), anchored on the granitic and gneissic bedrock of the Aar massif, exhibit long-term trends and cyclic displacements on top of some random noises (Oestreicher et al., 2021). To illustrate this observation, we select six topographic profiles, which pass through the six cGPS stations and transect from the mountain crest to the valley bottom (Figure 1). It can be seen that most of the cyclic displacements captured at the stations are constrained in the vertical plane of each corresponding profile. All stations except ALTD record outward displacement (positive in the longitudinal direction in green) from spring to early summer and inward displacement during late summer to winter. The annual cyclic vertical displacement is either small or below the noise level at most stations. This differs at station FIES, where the vertical displacement component exhibits a significant uplift of the station in spring and subsidence during the summer and fall. We note that FIES is situated closest to the ridge of the slope, while other stations are closer to the bottom of the valley or the current ice elevation (see Figure 1).

Figure 2 shows the daily position of each cGPS station through the year in the vertical plane of the profiles of Figure 1. The monthly average positions of the cGPS points (labeled with numbers) follow an annual hysteretic loop, with significant local variations between stations. Stations AL02, FIES, and ALTD are located on South-East facing slopes, while AL01, AL03, and ALTS are on North-West facing slopes. ALTD is the only station not displaying any significant annual cyclic displacement. Station AL02 moves approximately horizontally out of the slope in spring, with a fast motion in April and May. The peak displacement occurs in May. FIES starts its spring displacement in June and peaks in July before returning to its initial position at a lower speed during the summer and autumn. Between April and July, FIES moves upwards and outwards, 2.4 cm. FIES is located in the Fiesch valley at an elevation of ∼2350 m a s l, while AL02 is located in the Aletsch valley at ∼1950 m a s l, where the temperature is higher, and the snow melts earlier in the year. The three stations on the North-West facing slope of the Aletsch valley all show a similar pattern of fast spring displacement in May and June outwards, followed by a slower displacement back to its winter position (November to April). At station AL03, the displacement between February and July reaches 2.6 cm. The stations displaying annual cyclic motion have a slight counter-clockwise hysteresis, close to the noise level of the cGPS instruments outlined by the daily average positions (colored dots in Figure 2).

The rock mass structure has been assessed based on field and remote data aquisition methods. About 1400 fracture descriptions were manually recorded in the field, 134 outcrops were fully characterized for fracture sets and 6373 lineaments were traced from high-resolution orthophotos (see Figure 3) in the Aletsch valley. Subvertical joints parallel to the Alpine foliation form the primary set of persistent and closely spaced fractures, dipping to NW (Figure 3), (see also Grämiger et al., 2017). In addition, three joint sets are steeply dipping. Two of them are approximately perpendicular to the Alpine foliation; the third is dipping to S. These joint sets are often persistent, and the spacing between joints varies depending on the outcrop locations, in general around 0.4 m to 4 m. We identify two sets of flatter fractures with a larger spacing in the order of meters, one of them follows the current topography and is only identified on the left flank of the val-

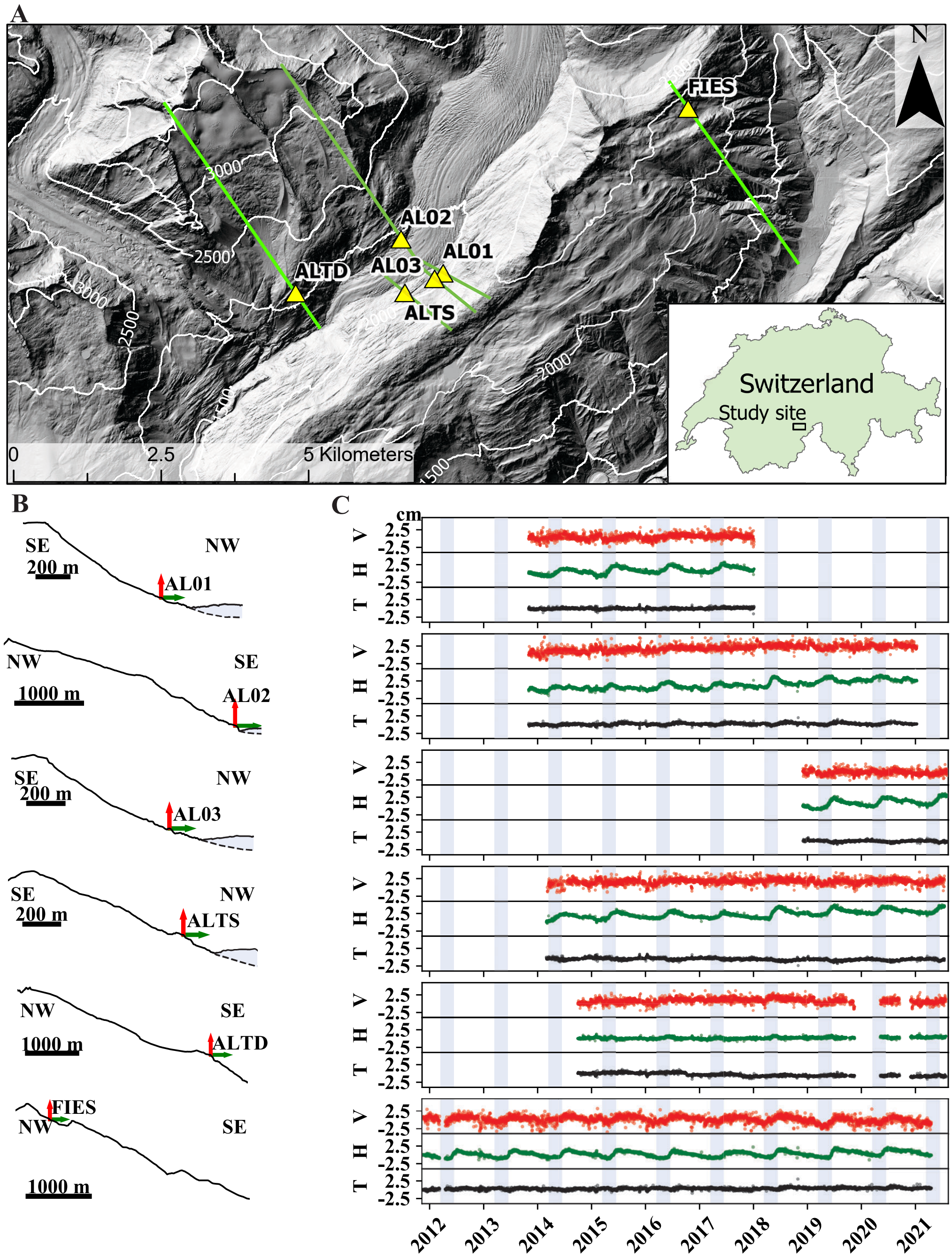

Figure 1. (A) Digital Elevation Model of the study area with 6 cGPS stations (yellow triangles) transected by (B) the selected 6 topographic profiles (green lines). Note that the Great Aletsch Glacier is represented in blue; the dashed line below the ice is the extrapolated bedrock surface to the center of the valley; the positions of the cGPS stations are at the intersection between the red and green arrows. (C) 3D displacement data of the cGPS stations, with red (V) being the vertical displacement, green (H) being the horizontal in-plane displacement (in the downhill direction), and black (T) being the out-of-plane displacement (towards the reader) in cm.

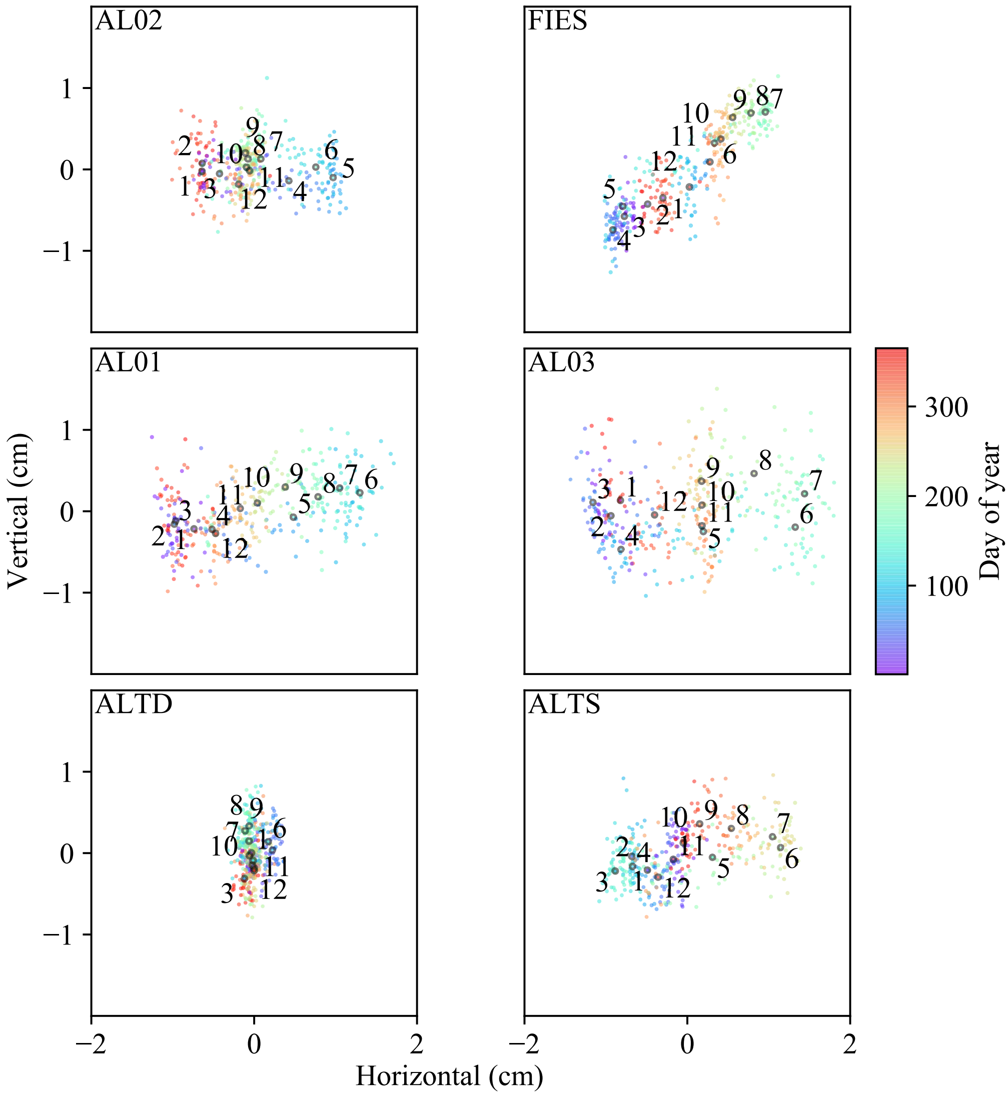

Figure 2. Annual motion in cross-section at each cGPS stations, in cm. Monthly average positions are points with a black outline, and colored points are daily average. Labels are months in the year.

ley. The other is found on both sides of the valley, often dips flatter than the current topography and the fractures' dip direction is predominantly SSW on the right flank of the valley and W on the left flank. We consider these two joint sets to be two generations of exfoliation joints. The orientation of larger lineaments (mainly brittle-ductile faults) is often parallel to the Alpine foliation. These subvertical NW dipping fractures (joints and faults) are suggested to strongly influence the infiltration and flow of the groundwater and participate in the rock mass deformation (Oestreicher et al., 2021). The lineaments can be traced on bedrock outcrops. Local Quaternary sediment cover from moraines and colluvial deposits inhibit fracture tracing from aerial images as well as during fieldwork (see Figure 3). The length of the lineaments is, therefore, sometimes underestimated due to the size of the outcrops. Below 2 m, fracture traces are under-sampled due to the extensive work needed to map smaller discontinuities at the valley scale and limitations due to the resolution of the orthophotos. The longest traces are around 1 km long and often consist of large-scale fault zones.

3 Numerical Methods

3.1 Problem Conceptualization

We develop numerical simulations to facilitate the interpretation of the underlying mechanisms of observed slope surface deformations. We construct a geological model (see Figure 4) to realistically represent fractured rock slopes in typical alpine mountainous environments. Note that we do not attempt to build a model to accurately reproduce the conditions at Aletsch valley, but rather aim to investigate the problem from a generic perspective. We discretize the domain (with a width of about 10 km) into a dense grid of blocks with the block size at the hectometer scale. We model the distribution of mesoscale fractures (e.g., with lengths smaller than the grid block size) based on the discrete fracture network (DFN) approach (Lei et al., 2017) with their impact on the rock mass properties of each grid block modeled through a homogenization paradigm. Large-scale fault zones (with lengths much larger than the grid block size) are not considered in the current model, and will be explored in a separate work; we will address the potential impact of large-scale fault zones in the discussion.

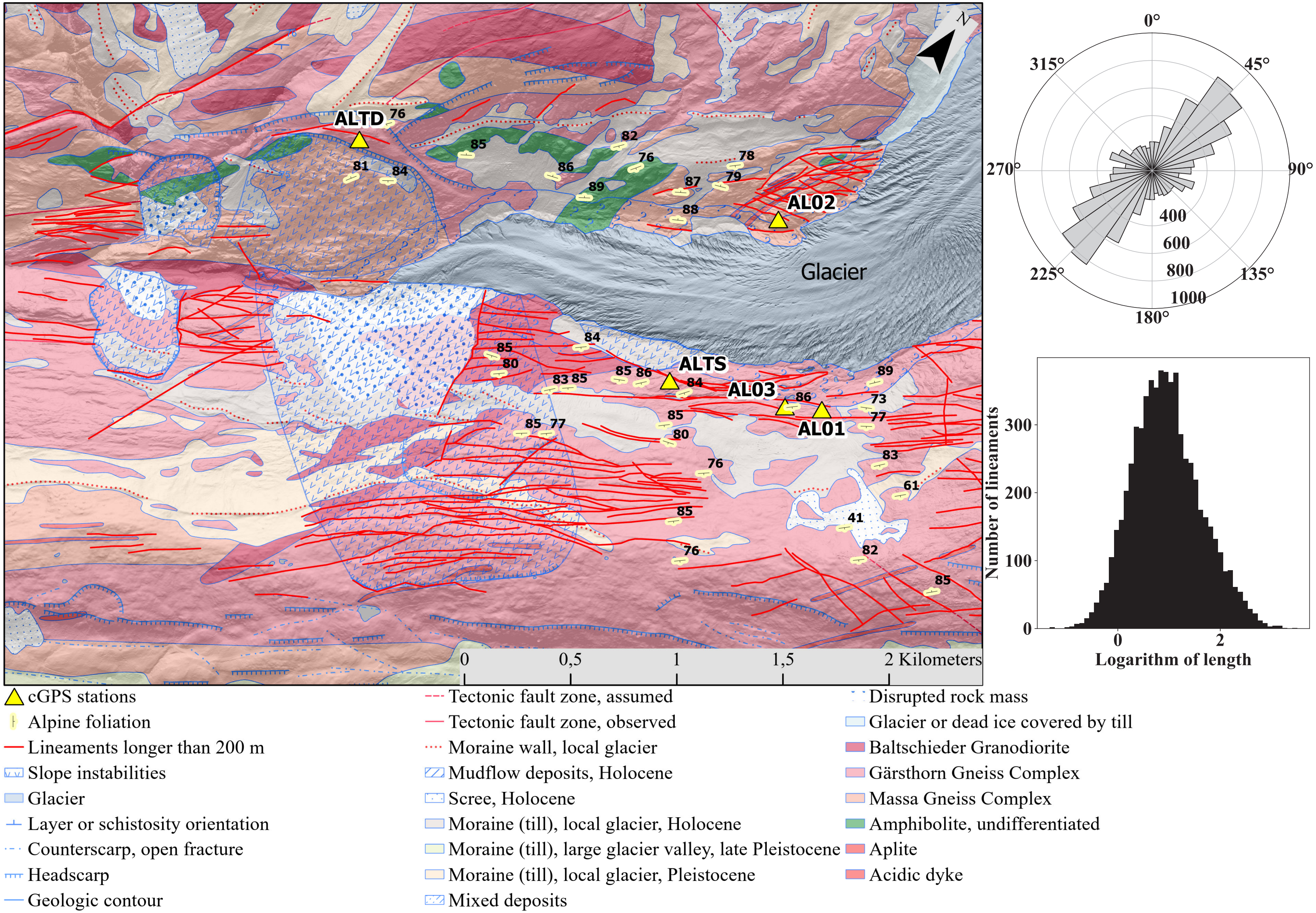

Figure 3. Geologic map of the study area, modified from Steck (2022) with lineaments longer than 200 m (red), the orientation of Alpine foliation with dip angle, and cGPS stations (yellow triangles). The rose diagram on the right shows the distribution of the lineaments' orientation; the histogram shows the lineaments' length (note the logarithmic scale).

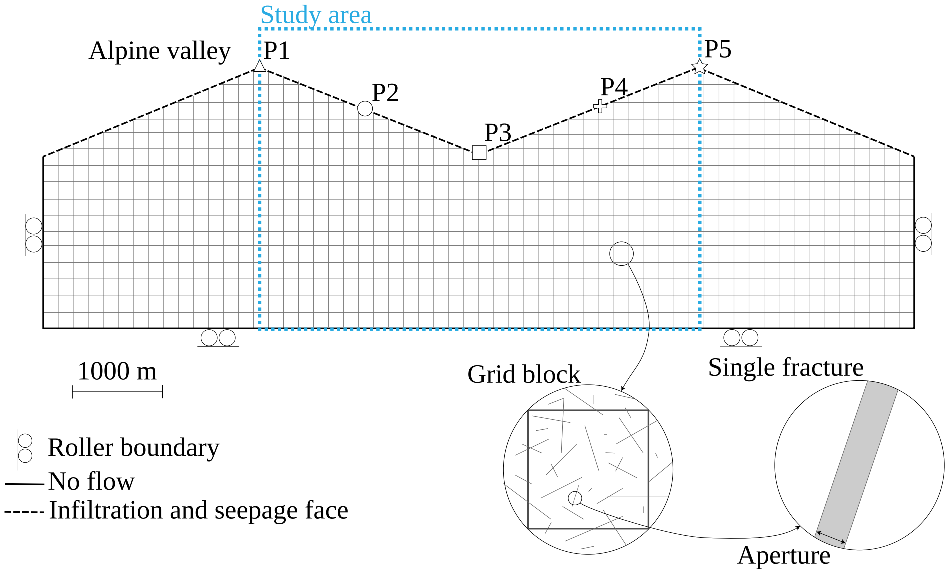

Figure 4. Schematic showing the model setup for the alpine valley simulation. The problem domain is discretized into a mesh of grid blocks assigned with equivalent properties taking into account the distribution of meso-scale fractures. The central dashed rectangle marks the study area.

204 ### 3.2 Geomechanics Model

The mechanical equilibrium of the fractured rock is governed by:

$$\boldsymbol{\nabla}\boldsymbol{\sigma} + \mathbf{f}_\mathrm{b} + \mathbf{f}_\mathrm{ext} = 0 \tag{1}$$

where $\boldsymbol{\sigma}$ is the total stress, $\mathbf{f}_\mathrm{b}$ is the body force, and $\mathbf{f}_\mathrm{ext}$ are the external forces such as boundary loads. The stress-strain relationship of the rock material obeys the linear poroelasticity law (Jaeger et al., 2007) given as:

$$\boldsymbol{\epsilon} = \mathbf{C} : \boldsymbol{\sigma'} = \mathbf{C} : (\boldsymbol{\sigma} - \alpha p \mathbf{I}) \tag{2}$$

205 where $\boldsymbol{\epsilon}$ is the strain, $\mathbf{C}$ is the compliance tensor, $\boldsymbol{\sigma'}$ is the effective stress, α is the Biot-
206 Willis coefficient, p is the pore pressure, and $\mathbf{I}$ is the identity matrix.

The closure behavior of a fracture under normal compression is governed by (Bandis et al., 1983):

$$v_\mathrm{n} = \frac{1}{1/v_\mathrm{m} + \kappa_\mathrm{n0}/\sigma'_\mathrm{n}} \tag{3}$$

where v_m is the maximum allowable closure, κ_n0 is the initial normal stiffness, and σ'_n is the effective normal stress (i.e., $\sigma'_\mathrm{n} = \sigma_\mathrm{n} - p$, where σ_n is the normal stress). For a fracture subject to shearing, the shear stress-shear displacement relationship is governed by Coulomb's friction law with the peak shear stress $\tau_{\mathrm{p}} = \sigma'_{\mathrm{n}} \tan\phi_{\mathrm{r}}$ where ϕ_{r} is the friction angle of the fracture. The shear displacement of the fracture walls τ_{s} could induce dilational displacement v_{s} which may be estimated as (Willis-Richards et al., 1996; Rahman et al., 2002; Ucar et al., 2017; Rutqvist et al., 2013; Gan & Elsworth, 2016):

$$v_{\mathrm{s}} = -\frac{|\tau_{\mathrm{s}}| - \tau_{\mathrm{p}}}{\kappa_{\mathrm{s}}} \tan\phi_{\mathrm{d}} \tag{4}$$

where κ_{s} is the shear stiffness, and ϕ_{d} is the dilation angle given by (Ladanyi & Archambault, 1969; Lei et al., 2020):

$$\phi_{\mathrm{d}} = \arctan\left[\tan\phi_{\mathrm{i0}}\ \left(1 - \frac{\sigma'_{\mathrm{n}}}{\sigma_{\mathrm{c}}}\right)^4\right] \tag{5}$$

where ϕ_{i0} is the initial dilation angle, and σ_{c} is the uniaxial compressive strength of the intact rock. The fracture aperture b_{f} is then calculated as (Lei et al., 2016):

$$b_{\mathrm{f}} = b_{\mathrm{f0}} - v_{\mathrm{n}} - v_{\mathrm{s}} \tag{6}$$

where b_{f0} is the initial aperture of the fracture (under zero stress).

For each grid block embedded with fractures, we compute the compliance tensor as (Oda et al., 1993):

$$\mathbf{C}_{\mathrm{ijkl}} = \sum^{N_{\mathrm{c}}} \left[\left(\frac{1}{\kappa_{\mathrm{n}} l} - \frac{1}{\kappa_{\mathrm{s}} l}\right)\mathbf{F}_{\mathrm{ijkl}} + \frac{1}{4\kappa_{\mathrm{s}} l}\left(\delta_{\mathrm{ik}}\mathbf{F}_{\mathrm{jl}} + \delta_{\mathrm{jk}}\mathbf{F}_{\mathrm{il}} + \delta_{\mathrm{il}}\mathbf{F}_{\mathrm{jk}} + \delta_{\mathrm{jl}}\mathbf{F}_{\mathrm{ik}}\right)\right] + \mathbf{C}_{\mathrm{ijkl}^{\mathrm{mat}}} \tag{7}$$

where N_{c} is the number of fractures within the block, κ_{n} and κ_{s} are the normal and shear stiffnesses of the fracture, respectively, l is the fracture length, δ_{ij} is the Kronecker's delta, $\mathbf{C}^{\mathrm{mat}}_{\mathrm{ijkl}}$ is the compliance tensor of the intact rock matrix, $\mathbf{F}_{\mathrm{ij}}$ and $\mathbf{F}_{\mathrm{ijkl}}$ are the so-called crack tensors derived as (Oda, 1986; L. Wang & Lei, 2021):

$$\mathbf{F}_{\mathrm{ij}} = \frac{l^2}{A_{\mathrm{b}}}\mathbf{n}_{\mathrm{i}}\mathbf{n}_{\mathrm{j}} \tag{8}$$

$$\mathbf{F}_{\mathrm{ijkl}} = \frac{l^2}{A_{\mathrm{b}}}\mathbf{n}_{\mathrm{i}}\mathbf{n}_{\mathrm{j}}\mathbf{n}_{\mathrm{k}}\mathbf{n}_{\mathrm{l}} \tag{9}$$

where A_{b} is the block area, and $\mathbf{n}_{\mathrm{i}}$, $\mathbf{n}_{\mathrm{j}}$, $\mathbf{n}_{\mathrm{k}}$ and $\mathbf{n}_{\mathrm{l}}$ are the directional components of each fracture.

3.3 Groundwater Flow Model

The continuity equation for single-phase fluid flow in fractured rocks is given by:

$$\frac{\partial(\rho_{\mathrm{w}}\varphi)}{\partial t} + \nabla\cdot(\rho_{\mathrm{w}}\mathbf{q}) = \mathbf{Q}_{\mathrm{s}} - \rho_{\mathrm{w}}\alpha\frac{\partial\epsilon_{\mathrm{v}}}{\partial t} \tag{10}$$

where ρ_{w} is the density of water, φ is the porosity, $\mathbf{Q}_{\mathrm{s}}$ is the source term, ϵ_{v} is the volumetric strain of the solid skeleton, and $\mathbf{q}$ is the flux defined in Darcy's law as:

$$\mathbf{q} = -\frac{\mathbf{k}}{\mu_{\mathrm{w}}}(\nabla p - \rho_{\mathrm{w}} g \nabla z) \tag{11}$$

where $\mathbf{k}$ is the permeability and μ_{w} is the dynamic viscosity of water. Furthermore, the storage behavior is governed by:

$$\frac{\partial(\rho_{\mathrm{w}}\varphi)}{\partial t} = \rho_{\mathrm{w}} S \frac{\partial p}{\partial t} \tag{12}$$

where S is the storage coefficient. The above equations (10)-(12) may be reduced to (Rutqvist & Stephansson, 2003):

$$\rho_{\mathrm{w}}\left(S\frac{\partial \rho}{\partial t} + \alpha \frac{\partial \epsilon_{\mathrm{v}}}{\partial t}\right) - \nabla \cdot \left(\frac{\mathbf{k}\rho_{\mathrm{w}}}{\mu_{\mathrm{w}}}\nabla p\right) = \mathbf{Q}_{\mathrm{s}} \tag{13}$$

For each grid block, the rock mass permeability tensor is calculated as:

$$\mathbf{k}_{\mathrm{ij}} = \frac{1}{12}\sum^{N_{\mathrm{c}}}(\mathbf{P}_{\mathrm{kk}}\delta_{\mathrm{ij}} - \mathbf{P}_{\mathrm{ij}}) + \mathbf{k}_{\mathrm{ij}}^{\mathrm{mat}} \tag{14}$$

where $\mathbf{k}_{\mathrm{ij}}^{\mathrm{mat}}$ is the permeability tensor of the intact rock matrix, and $\mathbf{P}_{\mathrm{ij}}$ is the crack tensor calculated as:

$$\mathbf{P}_{\mathrm{ij}} = \frac{b_{\mathrm{f}}^3 l}{A_{\mathrm{b}}}\mathbf{n}_{\mathrm{i}}\mathbf{n}_{\mathrm{j}} \tag{15}$$

4 Model Setup and Calculation Procedure

We construct a representative alpine valley with two symmetric valley flanks (highlighted by a dotted rectangle in Figure 4), bounded by two additional auxiliary valley flanks to minimize boundary effects. The model has an elevation change between the top and bottom of the slope of 1000 m and width from crest to crest of 5000 m. We consider a fluvial valley approximated as a smooth V shape with a slope angle of $\sim$21.8° (see Figure 4). To avoid lateral boundary effects, there are valleys symmetric to the one studied on the left and right sides, such that the model boundaries are always one valley away from the study area. The domain subject to gravity has the bottom constrained by a roller boundary condition, while the top is a free surface. The left and right are subject to a displacement control; a zero horizontal displacement corresponds to a roller boundary condition, and a non-zero value defines a prestrained condition increasing with depth; the vertical displacement is unconstrained.

For the groundwater flow model, we make an assumption that there is little lateral flow in the subsurface below the rivers forming the lateral boundaries of the model, so that we define the bottom as well as the sides of the model as no flow boundaries. At the surface, we model both the recharge process during periods of recharge and the seepage process at locations where the groundwater table reaches the ground surface (Chui & Freyberg, 2009; Grämiger et al., 2020):

$$-\mathbf{n}\rho\mathbf{u} = \rho(\chi_\mathrm{s} f_s + \chi_\mathrm{u}\frac{k_\mathrm{m}\rho_\mathrm{r} g}{\mu_\mathrm{w}} f_\mathrm{inf}) \tag{16}$$

where $\mathbf{n}$ is the normal to the surface, $\mathbf{u}$ is the fluid velocity, k_m is the permeability of the surface rock, ρ_r is the rock density, g is the gravitational force, f_inf is the recharge function and f_s is the seepage velocity function, χ_s and χ_u are the smoothing functions for the saturated and unsaturated parts of the boundary, respectively.

The material properties are listed in Table 1. The parameters are chosen to realistically represent a bedrock consisting of gneiss/granite embedded with small-scale (<5 m) fractures. Properties of the medium to large-scale fractures (<200 m) are also listed in Table 1. Two different approaches are applied to generate realistic fracture networks. In the first approach, we consider a system with a random orientation of fractures, and a depth dependency of the fracture density, as observed in many geological settings worldwide (Achtziger-Zupančič et al., 2017; Carlsson et al., 1983). The variation of fracture density follows an exponential function as:

$$d(z) = d_\mathrm{min}(d_\mathrm{max} - d_\mathrm{min})\exp(-\zeta\ z) \tag{17}$$

where z is the depth below surface, d_min the residual fracture density, d_max the maximum fracture density, and ζ is the density decay rate. In the base case model, we set the exponential decay factor ζ at 7.4×10^{-4} 1/m, the ratio $d_\mathrm{min}/d_\mathrm{max}$ at 0.1 and the total number of fractures in the model domain at 1×10^5. The distribution of fracture lengths follows a power-law:

$$n(l) = \omega\ l^{-a} \text{ for } l \in [l_\mathrm{min}, l_\mathrm{max}] \tag{18}$$

where ω is the density term, l_min the minimum length set at 2 m, l_max the maximum length set at 200 m, and a the power-law exponent (assumed as 2 in the current study).

In the second approach, we define the fracture system with systematic fracture sets. It allows us to define a set of subparallel fractures with the same depth-density relationship as above (see Equation 17) and dispersion of 0.62 rad and test the effect of the preferential orientation of hydraulically active fractures (i.e. fractures carrying water have a subparallel orientation, inducing a substantial rock mass anisotropy).

Table 1. Material properties of groundwater and fractured rocks

Properties	Symbols	Values	Units
Water			
Density	ρ_w	1000	kg/m^3
Viscosity	μ_w	8.9×10^{-4}	Pas
Compressibility	c_w	4.4×10^{-10}	1/Pa
Rocks			
Density	ρ_r	2700	kg/m^3
Initial porosity	φ_0	1×10^{-2}	-
Residual porosity	φ_r	1×10^{-3}	-
Uniaxial Compressive Strength	σ_c	150	MPa
Young's modulus	E_r	50	GPa
Poisson's ratio	ν_r	0.25	-
Initial permeability	k_r	1×10^{-19}	m^2
Biot-Willis coefficient	α_s	1	-
Fractures			
Initial aperture	b_0	0.01 - 1	mm
Maximum allowable closure	v_m	0.001 - 0.9	mm
Initial normal stiffness	κ_n0	20 - 60	GPa/m
Initial shear stiffness	κ_s0	10 - 30	GPa/m
Friction angle	ϕ_r	31	°
Initial dilation angle	ϕ_i0	5	°
Minimum fracture length	l_min	5	m
Maximum fracture length	l_max	200	m
Power-law length exponent	a	2	-
Density decay with depth	ζ	7.4×10^{-4}	-
Density ratio	$d_\mathrm{min}/d_\mathrm{max}$	0.01 - 1	-
Total number of fractures	N	5×10^4 - 2×10^5	-

We perform a series of simulations to explore the role of fractures in the groundwater flow and rock mass deformation, and the simulation results will be shown in Section 5. The first scenario is considered as the base case, with 1×10^5 fractures having an isotropic orientation, and a depth-dependent fracture density (residual density ratio $d_{\mathrm{min}}/d_{\mathrm{max}}$ of 0.1). The initial aperture of the fractures b_0 is set at 0.15 mm with a maximum allowable closure v_{m} at 0.135 mm, and an initial normal and shear stiffnesses of respectively 25 GPa/m and 12.5 GPa/m. To test the importance of the depth-dependent fracture density, we run simulations with various residual density ratios, from 0.01 (very strong density decrease with depth) to 1 (uniform density in the model, no depth-dependency) (see Section 5.2). We also analyze the effect of fracture anisotropy in a scenario where there is only one vertical set of fractures, with a random dispersion of the dip angle of 30° and a scenario with a set of oblique 45° inclined fractures, with a random dispersion of the dip angle of 30° too (Section 5.3). Then, we run a sensitivity analysis on the initial fracture aperture (Section 5.3). We also apply strain on the lateral boundaries to explore scenarios under higher tectonic confinements (Section 5.4).

The simulation runs in three consecutive stages. In the first stage, the pore pressure and mechanical loads are progressively ramped up in a stationary step. In the second stage, the model is run in a time-dependent manner and progressively brought to equilibrium by totaling nine recharge/depletion cycles. Finally, a last recharge/recession cycle is simulated. Only this last one is considered in this study to ensure that the model is at equilibrium and does not exhibit inter-annual trends in pore pressure change or surface deformation. We model a single annual recharge step representing groundwater recharge in response to snowmelt. The other smaller recharge events during the rest of the year are considered by applying a constant minimum recharge rate of a third of the recharge rate during snowmelt. The snowmelt recharge pulse starts at 35 % and stops at 60 % of the year, corresponding roughly to the period between May and early August in the Northern hemisphere. The maximum recharge rate is taken as ~1.1 mm/d, corresponding to a total yearly water amount of 0.1 m. Considering a recharge rate of ~10 %, the precipitation needed is around 1 m/y which is a reasonable amount for typical alpine environments (Markovich et al., 2019).

We discretize the problem domain using an unstructured mesh of triangular elements with the maximum element size of 60 m and a refinement at the top surface (with

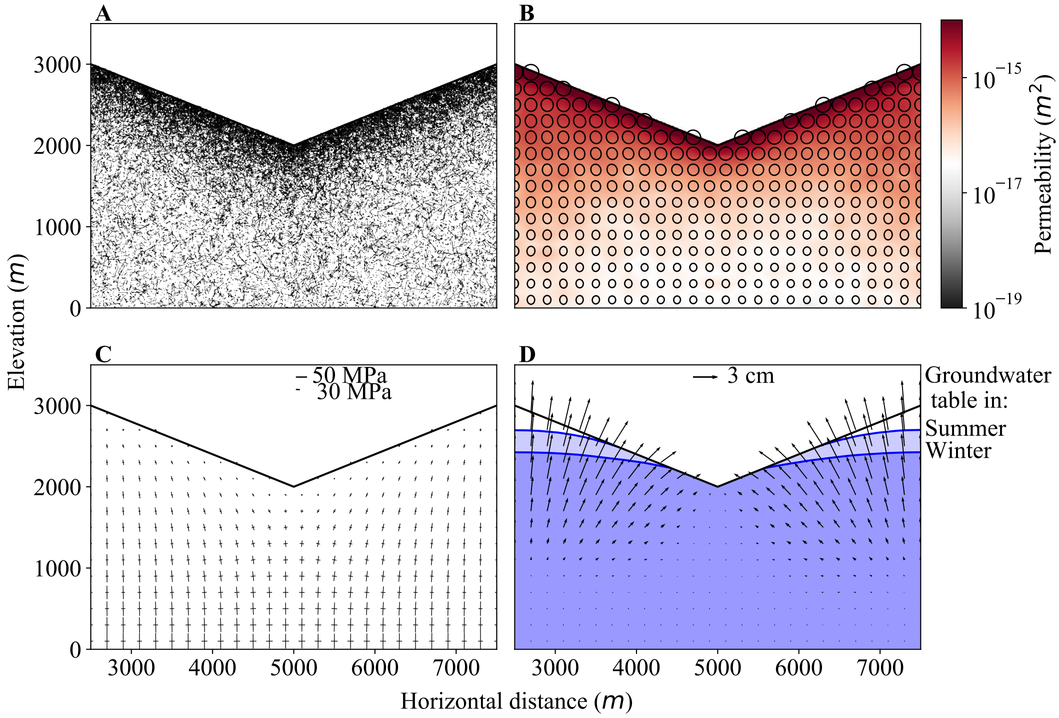

Figure 5. Model with random fracture orientations and depth-dependent fracture density. **A:** Generated discrete fracture network. **B:** Permeability field, with permeability ellipses scaled with the logarithm of the permeability magnitude. **C:** Stress modeled in the valley (the length and orientation of each line represent the magnitude and orientation of principal stresses, respectively). **D:** Observed change in groundwater table before and after the spring snowmelt recharge and corresponding displacement observed in the rock mass between these two instants.

a size of 5 m). The solver adapts the simulation time step with a maximum step of 1 d during periods of recession and 0.1 d during periods of recharge.

5 Simulation Results and Analysis

5.1 Pore Pressure-Driven Displacement in Fractured Rock

In the scenario that we define as the base case in this paper, rock masses exhibit an exponentially decaying areal fracture intensity (P21) with depth (Figure 5A), varying from around 20 m/m^2 at the near-surface to around 12 m/m^2 in the deep subsurface. The permeability also decreases from a value of around 2×10^{-14} m^2 at the near-surface to a much lower permeability of $\sim1\times10^{-17}$ m^2 in the deep subsurface (see Figure 5B). The permeability is strongly affected by local stress conditions, which control fracture normal closure and shear dilation behaviors. The principal directions of the stress tensor are shown in Figure 5C and exhibit a rotation from parallel to the topography (reverse faulting, horizontal over vertical stress ratio between 1 to 5) in the near-surface to vertically oriented in the deep subsurface (strike-slip faulting regime, with stress ratio ranging between 0.3 to 1). The effect of local stress state on rock mass permeability can be further visualized in Figure 6, where the permeability is generally lower for an observation line below the center of the valley (P3, see Figure 4) compared to those observation lines in the middle of the slopes (P2 and P4) or below the crests (P1 and P5). Figure 5D shows the variation of groundwater table in the rock mass between the low water level time (before the start of the main recharge pulse) and the high water level time (at the end of the main recharge period). The phreatic surfaces of both water level conditions are the blue curves; the area that is permanently saturated is in dark blue, while the area where the water table fluctuates is colored in light blue (see Figure 5D).

The displacement field is also shown in Figure 5D, where black arrows illustrate the orientation and magnitude of ground displacement between the start and end of the recharge period. The deformation is systematically oriented towards the center of the valley and upwards during recharge events. The maximum displacement amplitude is of centimetric level at the mountain crest (up to 3.4 cm) and appears negligible near the valley bottom. At the mountain crests, the deformation is mostly subvertical. For points at the surface between these two limiting locations, we observe a progressive rotation of the displacement direction, passing through horizontal and oriented towards the center of the valley around the points where the slope is permanently fully saturated and oriented upwards for points higher in the slopes (see Figure 5D).

The displacement changes over time, simultaneously with the diffusion of the recharge-related pore pressure front migrating from the top of the mountain crests to the bottom of the domain and laterally to the valley center, where discharge occurs (see Figure 7). During recharge, most of the deformation is concentrated in the top region of the domain (see Figure 7A), and the surface displacement is more significant in the top half of the slope than near the valley bottom. The orientation of the displacement is vertical upwards close to the crests, but rotates to horizontal around the bottom of the slope and is even oriented downwards at the center of the valley. At the end of the recharge period, the displacement reaches its maximum at the surface (see Figure 7B). Points in the bottom half of the slope start to rotate and point upwards. We see a transfer of the

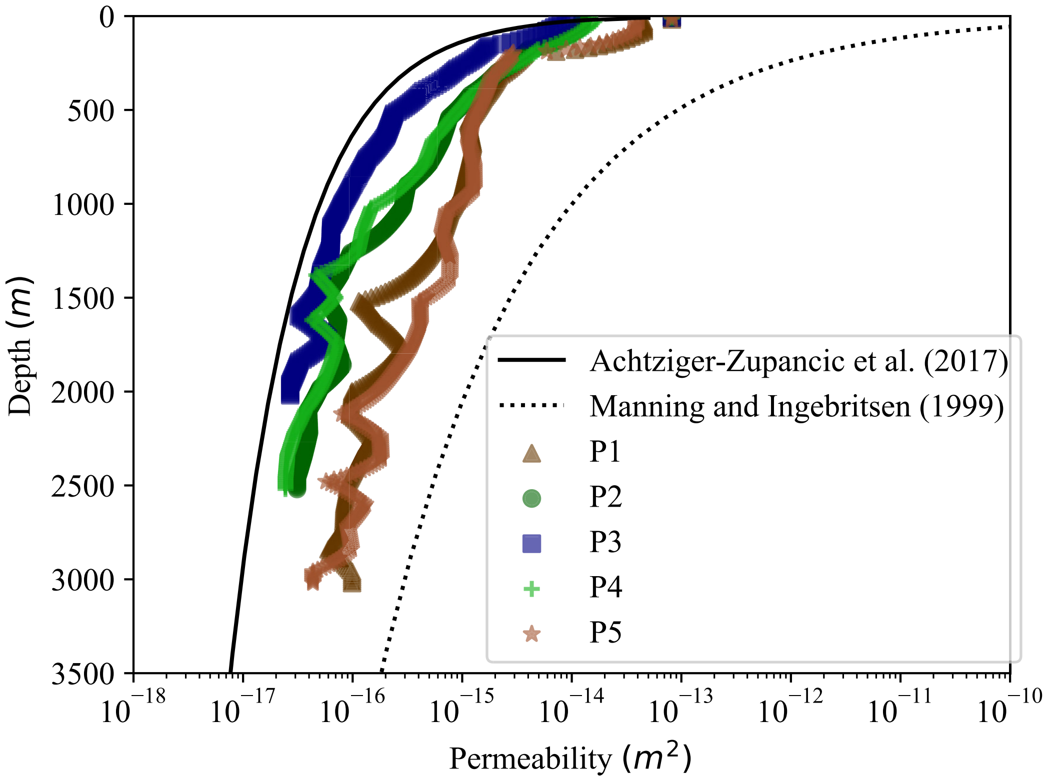

Figure 6. Vertical permeability profiles below the five points displayed in Figure 4. The continuous black line is the equation from the field measurements of permeability in crystalline rocks worldwide from Achtziger-Zupančič et al. (2017), and the dashed black line is the equation from the dataset of Manning and Ingebritsen (1999).

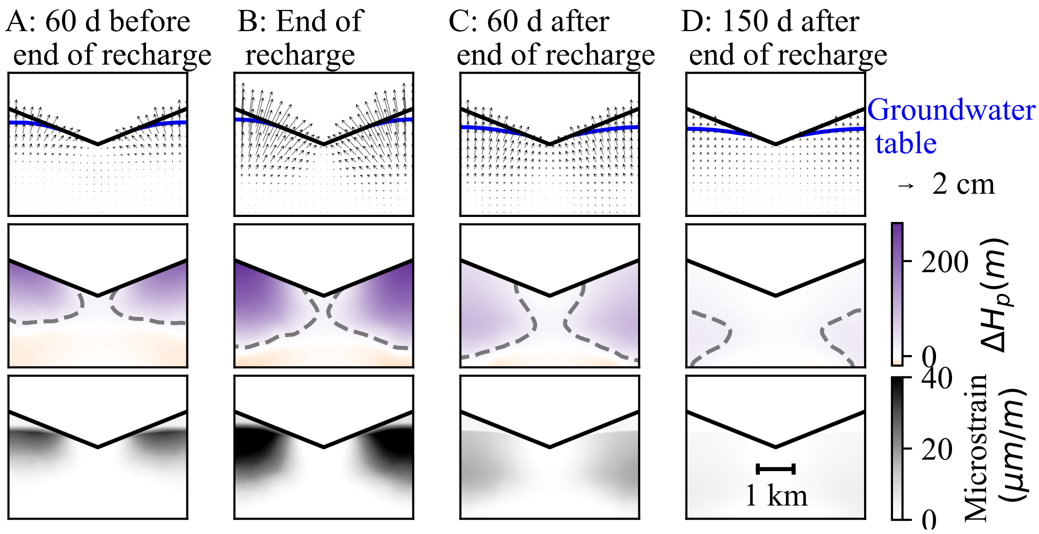

Figure 7. Selected times for comparison with low water table conditions before the recharge starts. The first row shows the displacement field relative to the start of the recharge (black arrows, whose length is the magnitude of the deformation) and the groundwater table (continuous blue lines). The second row shows the head pressure difference relative to the low water table conditions. The pore pressure plume is in purple (dashed line is 20 m contour line, delimited to help the reader visualize the propagation of the pore pressure diffusion front). The last row shows the corresponding deformation field in microstrain ($\mu m/m$).

strained rock mass to deeper zones, together with the diffusion of the pore pressure plume. After the end of recharge, the pore pressure plume diffuses to the deepest parts of the domain and laterally to the center of the valley (see Figure 7C). Rapidly, the differential pore pressure is reduced. However, the pore pressure anomaly is preserved at the end of the recharge in the bottom part of the system. During the recession period, the surface displacement magnitude is strongly reduced, and the displacement direction progressively rotates upwards (see Figure 7D). Figure 8 shows the displacement data at the three control points P1, P2, and P3, for a full cycle of recharge and recession. The displacement at the crest and valley bottom is predominantly vertical. However, the logarithmic scale helps to detect a minor hysteresis caused by a small random asymmetry in the fracture network on both sides of the control points (see Figure 8). At the mid-slope, the hysteresis is much larger, with a displacement of the control point out of the slope during recharge and an upwards rotation during the recession (see Figure 8).

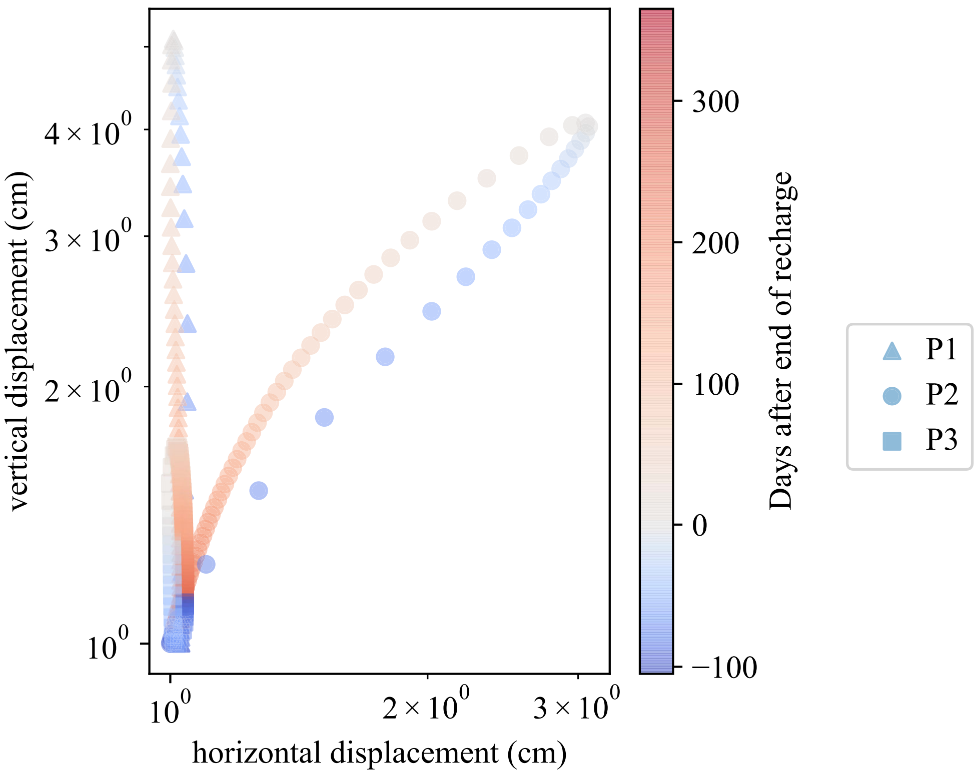

Figure 8. Displacement during a cycle of recharge and recession at the three control points P1, P2, and P3 shown in Figure 4. The recharge is in blue, the recession in red, and the transition at the end of the recharge in grey. Both scales are logarithmic, and the data is transformed by removing the minimum value of the timeseries and adding 1 cm.

5.2 Effect of Fracture Network Geometry

The model with a uniform fracture density distribution (i.e., without depth dependency) also shows a marked decrease of the rock mass permeability with depth, varying from around $5 \times 10^{-14}\,\mathrm{m}^2$ near the surface to $1 \times 10^{-16}\,\mathrm{m}^2$ at great depth, due to the variation of in-situ stresses with depth. In comparison to the base model presented in Section 5.1, a model with uniform fracture density has larger permeability at depth. This results in smaller ($\sim$100 m) groundwater table variations during a recharge/recession cycle (see Figure A6 in appendix) compared to the base model. The smaller pore pressure fluctuations observed in the rock mass lead to a smaller magnitude of the seasonal deformation. The maximum displacement observed during the recharge for the model with a uniform fracture density distribution is 6 mm while it is 36 mm for a model with the density ratio $d_{min}/d_{max} = 10\,\%$ and even 42 mm for a model with $d_{min}/d_{max} = 5\,\%$ (see Figure A6 in appendix). The density decrease with depth also influences the orientation of the displacement. We observe that the vertical displacement is more sensitive to the variations of the residual density ratio than the horizontal displacement, as captured by the points in the middle of the slopes. This effect is more pronounced for a density ratio smaller than 20 %, where the changes in displacement magnitudes are also more significant. For a residual density ratio above 20 %, the horizontal displacement magnitude is in general consistently around 1.5 times larger than the vertical one (see Figure A6 in appendix).

Figure A1A shows the fracture network for a scenario with a single hydraulically active fracture set, where fractures are oriented vertically with a dispersion of 10°. In such a case, the permeability field exhibits a strong anisotropy, where the vertical component of the permeability tensor is significantly larger than the horizontal one (see Figure A1B). In comparison with the base case (Section 5.1), the groundwater table elevation changes (up to 150 m below the crests) are reduced in the case of a model with solely vertical fractures (both models have the same number of fractures in the rock mass and the same depth-dependent density decrease). The downwards-oriented displacement below the center of the valley is of smaller magnitude. The displacement at the valley's surface has a lower dip angle and a lower magnitude (approximately −20 %) than that in the model with randomly oriented fractures. For a model with a set of 45° inclined fractures, the displacement at the surface is asymmetric, with the crest deforming in a direction parallel to the strike of the fractures (see Figure A3). Due to the strongly anisotropic permeability field, the water from the recharge diffuses from the crest preferentially following the fractures, and induces a large deformation only on that side of the valley. The other valley flank has a significantly lower permeability (see Figure A3B), and significantly less surface displacement (see Figure A3D). In conditions where a single fracture set dominates the rock mass discontinuity pattern (e.g., Figure A1 and Figure A3), the strongly preferred orientations of hydraulically active fractures in the rock mass result in an anisotropy of the rock mass permeability. This anisotropy in permeability leads to smaller groundwater table elevation changes and pore pressure variations and higher groundwater table elevations in the slope. In parallel, the anisotropic elasticity of rock masses also affects the slope's displacement. With a set of vertical fractures, as shown in Figure A1, there is a zone ($\sim$200 m deep below the valley bottom and $\sim$1200 m deep below the crests) where the slope deforms around 6 % to 12 % more in the vertical direction than in the horizontal direction. This is because the shear stiffness of fractures is typically lower than their normal stiffness.

5.3 Effect of Fracture Aperture and Rock Mass Permeability

We further evaluate the impact of fracture initial and residual aperture and stiffness, which exert a major control on the rock mass permeability (e.g., for the initial aperture variation of 0.1 mm to 1 mm the observed permeability varies by around three orders of magnitude; see Figure 9). The increase in permeability is not homogeneous in space and is particularly significant close to the surface, where the permeability is higher (see Figure A5A in the appendix). Normalizing the permeability change with the original permeability reveals that the largest relative permeability difference is at depth below the valley and minimal near the mountain crests (see Figure A5B in the appendix). Figure A5 shows that the relationship between the initial fracture aperture and the permeability is not trivial. To better compare the results of the models with different initial fracture aperture values, we analyze the time series of pore pressure and displacement at the five control points as marked in Figure 4.

In Figure 10, one can see that the groundwater table follows a similar trend for all control points if the initial aperture is large (e.g., 1 mm), showing an increase during the recharge followed by a gradual decrease during the recession period. The maximum groundwater level is reached at the end of the recharge (see the red dashed line), and the minimum level is reached at its start (see the blue dashed line). Decreasing the initial frac-

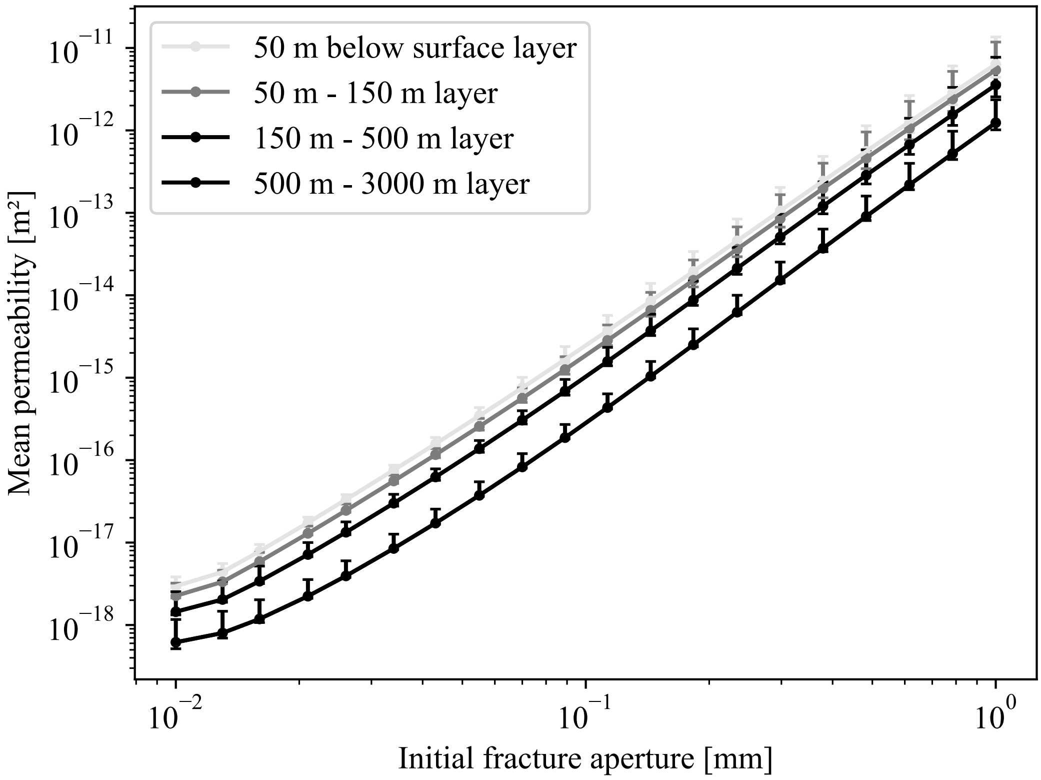

Figure 9. Arithmetic mean permeability per depth intervals in the entire model domain, when varying the initial aperture of the fractures in the rock mass, in logarithmic scales. Darker colors are for deeper zones of the model domains below the surface.

ture aperture (and thus, the rock mass permeability) strongly affects the groundwater table and its fluctuations. We observe that the groundwater table elevation difference between control points at a given time increases with a reduced fracture aperture.

The horizontal displacement shown in Figure 10F to 10K is negligible in a system with large fracture initial apertures. The average change in hydraulic gradient between low and high water conditions is relatively small (0.09 for an initial fracture aperture of 1 mm). With the decrease of fracture aperture, we observe that the horizontal displacement becomes more significant (>1.5 cm) for points in the middle of the slope (P2 and P4) while remains small for points at the crests (P1 and P5) and valley bottom (P3). The hydraulic gradient varies also more (0.12 for an initial fracture aperture of 0.15 mm). The displacement between the start and end of the recharge period is positive at P2 and negative at P4, i.e., oriented towards the center of the valley (see Figure 10G and 10I). The vertical displacement exhibits a strong uplift at all control points during the recharge for models with large initial fracture aperture values (Figure 10L to 10P), but the uplift is strongly reduced in systems with small initial fracture aperture values at mid-slope and below. At the valley bottom (P3), for a particularly small initial fracture aperture (say below 0.2 mm), the effect is reversed, and the control point exhibits minor subsidence during the recharge period. As the initial fracture apertures (and hence rock mass permeability) are reduced, the pore pressure hydraulic front extends less far down in the slope. Therefore, the zone with elevated pore pressure changes during recharge impacts a smaller volume of rock mass, which impacts the surface deformation.

In Figure 11A, the groundwater table elevation at the end of the recharge period (red dashed line in Figure 10) exhibits an increase in groundwater table gradient in the slopes for systems with lower initial fracture aperture. The pore pressure changes (Figure 11B) reach a maximum of 250 m below the mountain crests for the scenario with an initial fracture aperture of 0.2 mm. For scenarios with a larger initial aperture, the groundwater table changes progressively converge towards a value of 100 m; for smaller initial apertures, the magnitude of changes decreases for all control points (see Figure 11B). The horizontal and vertical displacements are also shown in Figure 11C, and D. Most of the horizontal deformation happens for a small range of initial fracture aperture. At low initial fracture apertures (when the groundwater head changes decrease in Figure 11B), both the horizontal and vertical components of the deformation are negligible. At large initial fracture apertures (when the groundwater head changes converge to 100 m, and

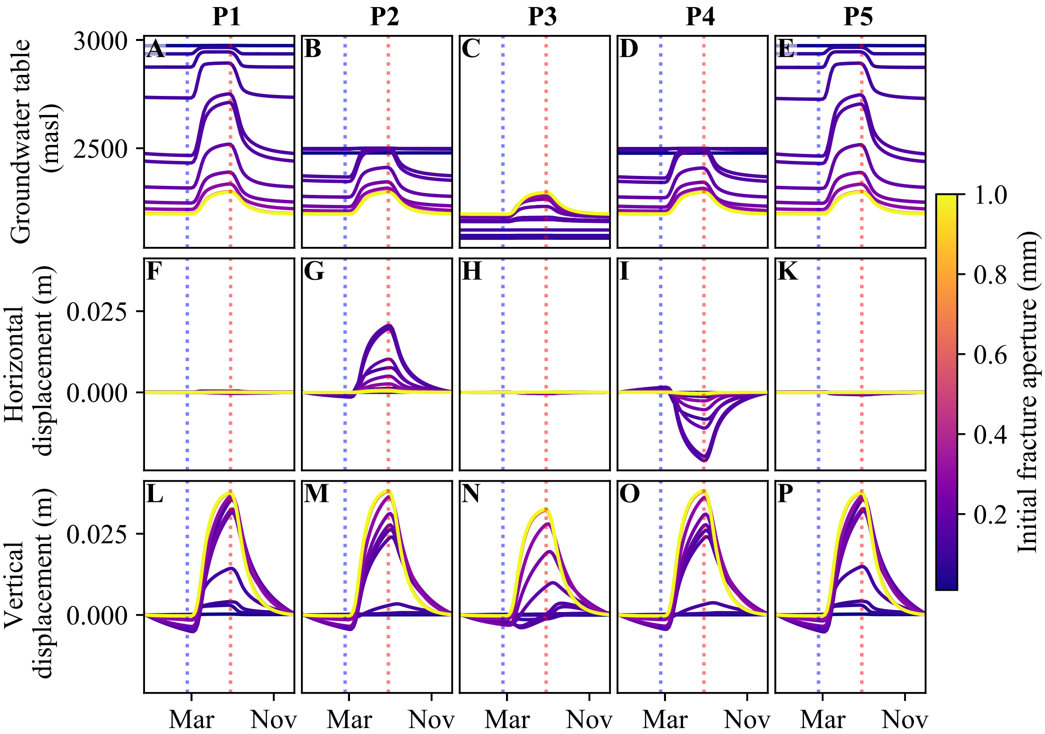

Figure 10. Groundwater table and displacement time series over 1 y as recorded at five control points (see Figure 4 for their locations; P1 and P5 are at crest positions, P2 and P4 are at the mid-slope, and P3 is at the valley bottom). The dotted lines are the recharge period's start (blue) and end (red). The color of the curves indicates the value of initial fracture aperture. A-E: Time series of groundwater table elevation; F-K: Horizontal displacement at control points; L-P: Vertical displacement at control points.

the hydraulic gradient is small in Figure 11A), the vertical component of deformation is strongly dominant, and the entire valley is uplifted during recharge.

5.4 Effect of Regional Stress Field

We investigate the effect of regional stress conditions by progressively increasing the strain at the lateral model boundaries. The stress field in the model domain then varies, and the ratio between horizontal and vertical stress increases locally (see Figure 12). The change in stress ratio is particularly marked close to the valley center, and the area of the domain that is in a reverse faulting regime (with the horizontal stress larger than the vertical one) progressively increases until covering the entire domain (see Figure 12). We also observe a decrease in permeability as the lateral confinement increases, particularly in the valley center's proximity.

The groundwater pressure changes during recharge decrease when confinement is added, with a larger change for small values of strain values (see Figure 13B). The observed displacement decreases as well, but the vertical displacement is more impacted than the horizontal one (see Figure 13C and D). Therefore, the ratio between horizontal and vertical displacement increases with the increase of the lateral confinement strain (see Figure 13E). The ratio between displacement magnitude and groundwater head change in Figure 13F generally decreases with the increasing lateral strain. A system under higher confinement, therefore, produces less surface deformation for a given head change. The maximum depth of the pore pressure diffusion front also decreases with the lateral confinement increase.

6 Discussion

6.1 Mechanisms of Pore Pressure-Driven Slope Deformation

Several previous studies documented that fractured bedrock slopes deform in response to groundwater recharge. Here we study the underlying mechanisms of this phenomenon with a new fully coupled fracture network model and compare the results of this generic model to observations in our study area of the Aletsch region, where we implemented a unique monitoring system, which allows to explore the detailed surface displacement vector orientations and magnitudes in space and time. In the Aletsch study area, the valley slopes deform annually by about 1 cm to 3 cm in response to high snowmelt-

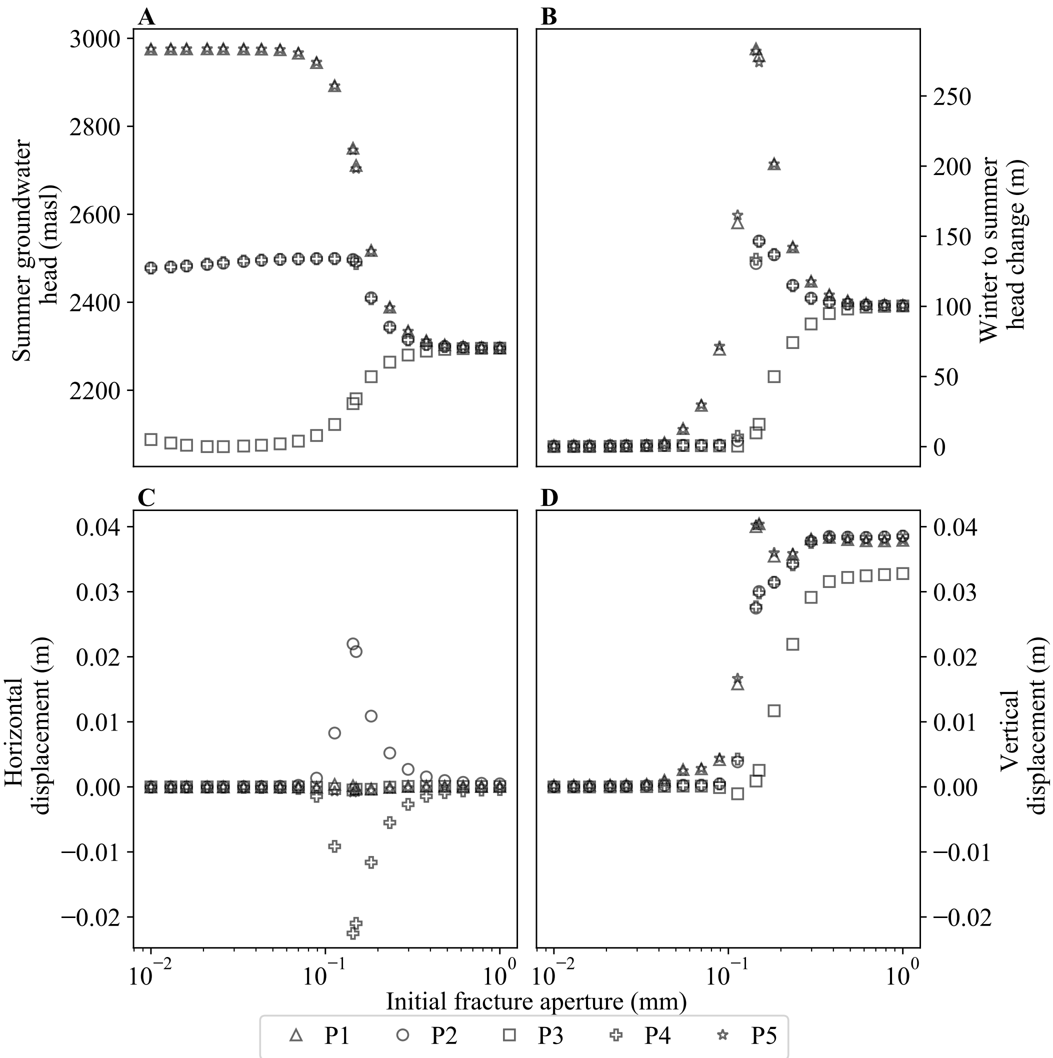

Figure 11. Effect of initial fracture aperture on groundwater table fluctuations and displacement at the five control points from Figure 4 between start and end of recharge (red and blue dashed lines in Figure 10). A: Groundwater table elevation in high water table conditions; B: Groundwater table elevation changes between start and end of recharge; C: Horizontal and D: vertical displacement between start and end of recharge.

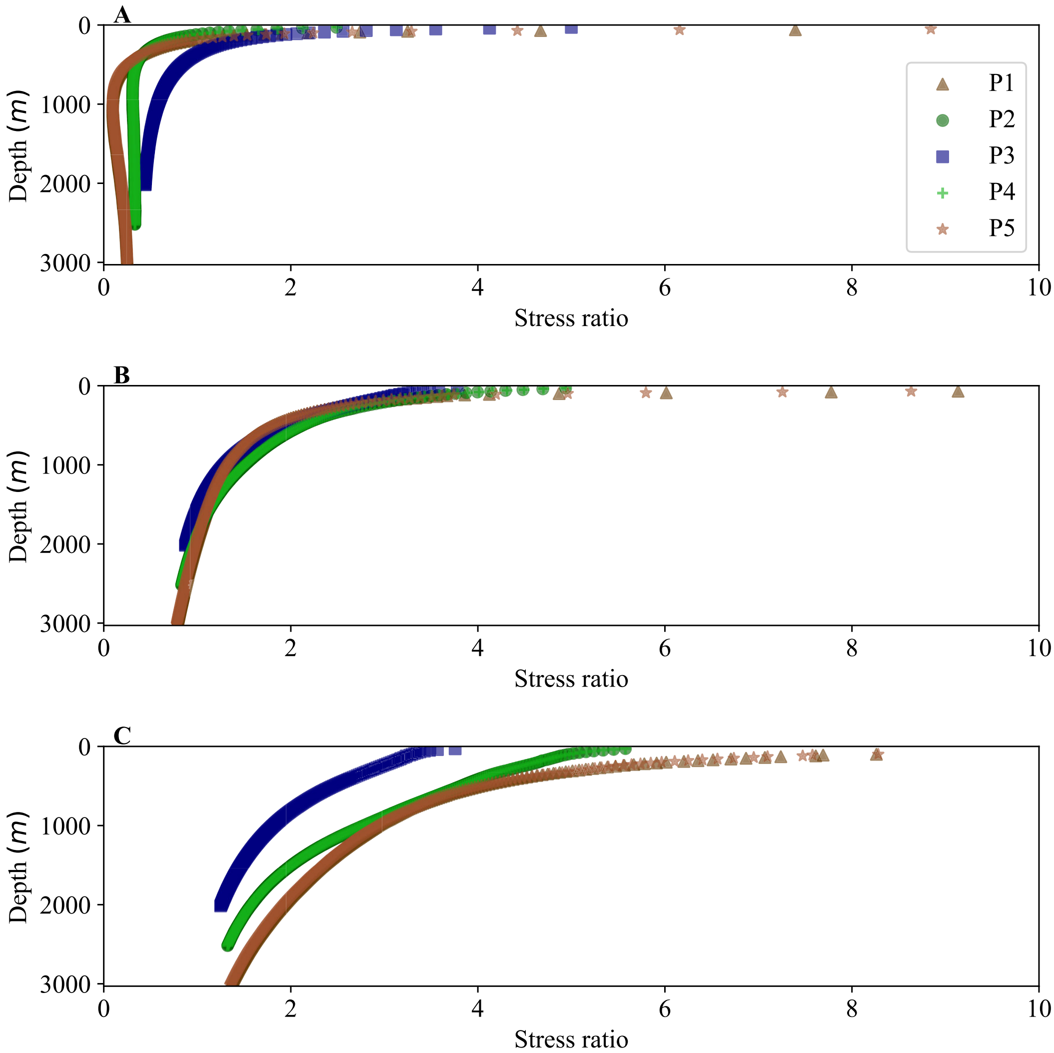

Figure 12. Strain ratio for the 5 vertical lines below the control points from Figure 4 in the cases of an additional lateral strain of 0 ms (A), 4 ms (B), and 8 ms (C).

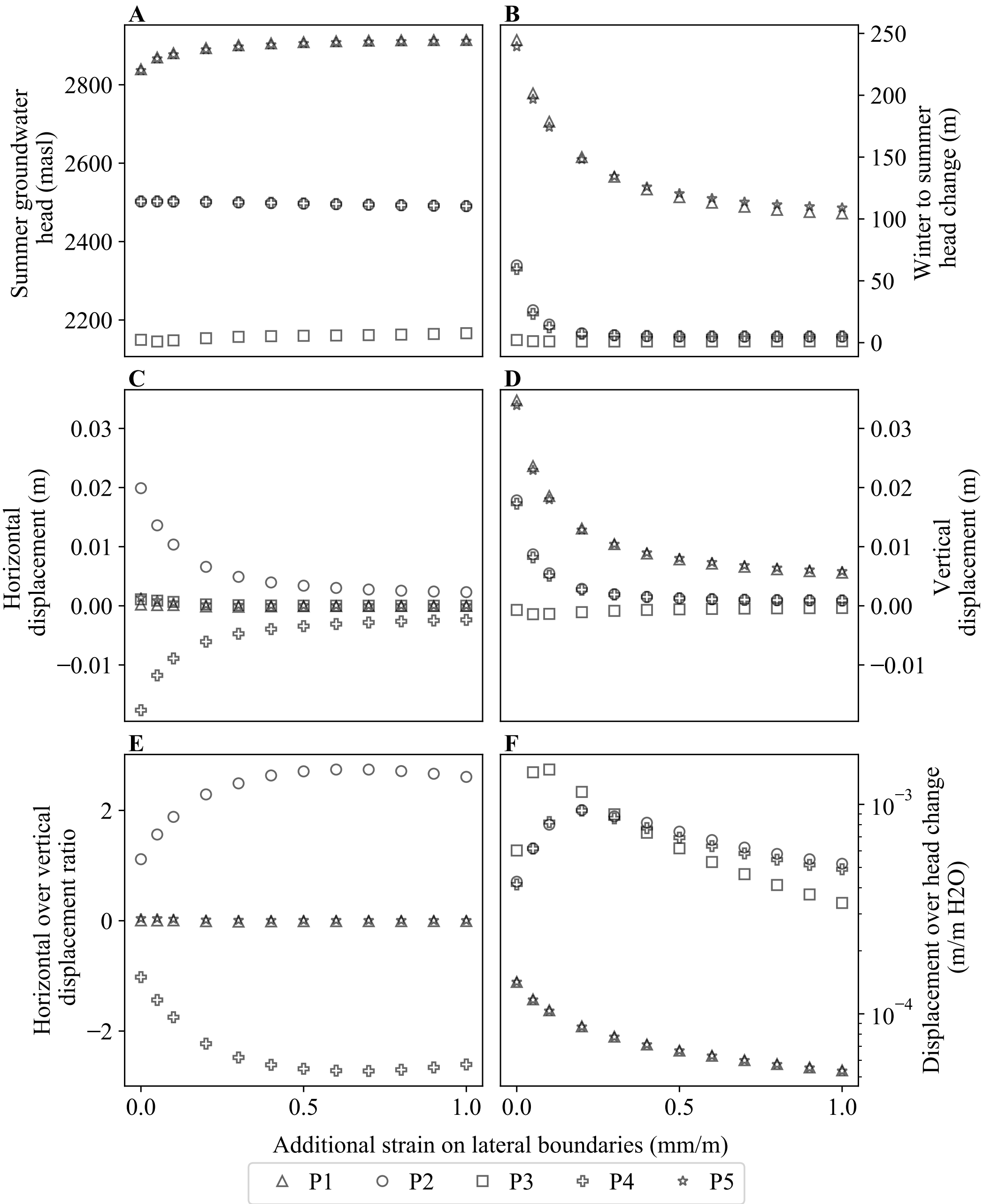

Figure 13. Effect of lateral stress on groundwater table fluctuations and displacement at the five control points from Figure 4 between start and end of recharge. A: Groundwater table elevation in high water table conditions; B: Groundwater table elevation changes between start and end of recharge; C: Horizontal and D: vertical displacement between start and end of recharge; E: Ratio of horizontal and vertical displacement in C and D; F: Displacement magnitude (from C and D) over groundwater table elevation changes (B) in logarithmic scale.

related recharge intensity occurring during spring (Oestreicher et al., 2021), and groundwater flows through joints and faults in granites and gneisses (see Figure 1 and Oestreicher et al. (2021)). In section 5, we showed how the signals monitored at the ground surface result from multi-scale hydromechanical processes operating from the fracture scale to the hillslope scale, where fracture density, orientation, aperture, and regional stress distributions play a critical role in controlling the flow and displacement dynamics. Here, we discuss and generalize the main insights into hillslope-scale coupled processes gained from our numerical investigations.

The transient ground surface displacements follow a complex hysteretic path related to the progressive propagation of the pore pressure front following the recharge event. The pressure front diffuses from the main recharge location at the mountain crest towards the seepage zone in the lower part of the mountain slope. The typical depth range of this hydraulic response zone causing subsurface strain and ground surface displacements is about two times the valley topography, reaching substantially below the valley bottom. Thus, the surface displacement orientation and magnitude depend on the location and shape of the hydraulic response zone within the first few hundreds of meters below the surface and evolves through time (see Figure 7).

The most important factor controlling the direction and amplitude of surface displacements is the subsurface rock mass permeability pattern and anisotropy. Several studies have defined a "hydraulically active region" with increased permeability and Darcy flow down to 200 m to 500 m depth (Welch & Allen, 2012; Gleeson & Manning, 2008; Ofterdinger et al., 2014; Markovich et al., 2019). In our model, we imposed a decrease in permeability with depth which results from the combined effect of increasing stress level (see Section 5.2) and decreasing fracture density (e.g. Manning & Ingebritsen, 1999; Achtziger-Zupančič et al., 2017). Furthermore, as we show, the change of permeability depends on the topography, with a stronger permeability decrease with depth below the valley than below the mountain crests due to local topography-driven stress variations (see, for example, Figure 6 and Figure 5). The depth-permeability relationship exerts a strong control on the depth and magnitude of the pressure change in the hydraulic response zone causing the surface displacements. A stronger decrease in permeability with depth results in significantly larger surface deformations due to larger groundwater table variations, but also more horizontal deformation at the mid-slope (see Figure A6).

A low near-surface (<150 m) permeability in the range of 1×10^{-15} m^2 and smaller (e.g., with initial fracture aperture <0.09 mm in Figure 11) keeps the groundwater close to the ground surface and does not allow significant pore pressure changes at depth; hence, it is associated with negligible deformations (see Figure 11). This permeability is typical for aquitards where potential recharge is greater than permeability, such as in tight crystalline rocks or shales. A high permeability in the near-surface layers of more than 1×10^{-13} m^2 (e.g. with initial fracture aperture >0.3 mm in Figure 11) drives rapid groundwater flow at depth and a flatter groundwater table (see Figure 11A), associated with vertical deformation and little horizontal displacement at the surface. Only between these two cut-off values, i.e., in a narrow permeability range close to the magnitude of annual recharge, we observe significant variations in phreatic groundwater level elevation. Here, magnitudes of induced ground surface displacements are observable by conventional monitoring systems, and the hydraulic response zone takes the shape of an elongated zone below the mountain crests (see Figure 7B) and diffuses downwards and laterally during and after the recharge event. Our model shows that the magnitude of the groundwater table variations is not linearly related to the permeability changes in slopes, as exemplified by varying the initial fracture aperture for all fractures in the model. The change of regime is relatively sharp at an initial fracture aperture between ∼0.08 mm to 0.3 mm (see Figure 11B) and leads to larger groundwater table variations and larger horizontal displacement at the mid-slope.

For models with a strongly preferred fracture orientation, we observed strong anisotropy in both the rock mass permeability and the surface displacement pattern (see Section 5.2). Such observations are consistent with small-scale studies (Tsang et al., 2007; Noorian Bidgoli & Jing, 2014; Ren et al., 2015). We can formulate two different possible mechanisms to explain the observations. First, the anisotropic deformation of the rock mass may be solely due to the anisotropic elasticity of the rock. Indeed, the presence of discontinuities in the rock mass is shown to strongly impact its deformation modulus (Hoek & Diederichs, 2006), and the organization of the fracture network dominated by a single fracture set naturally results in a strong anisotropic elasticity (Barton, 2013). Second, the anisotropic deformation of the rock mass may be the result of the hydromechanical forcing. In this case, the presence of the fracture set induces an anisotropy in permeability (e.g., Rutqvist & Stephansson, 2003), modifying the hydraulic response zone at depth. The change in the shape of the hydraulic response zone then impacts the rock mass deformation field

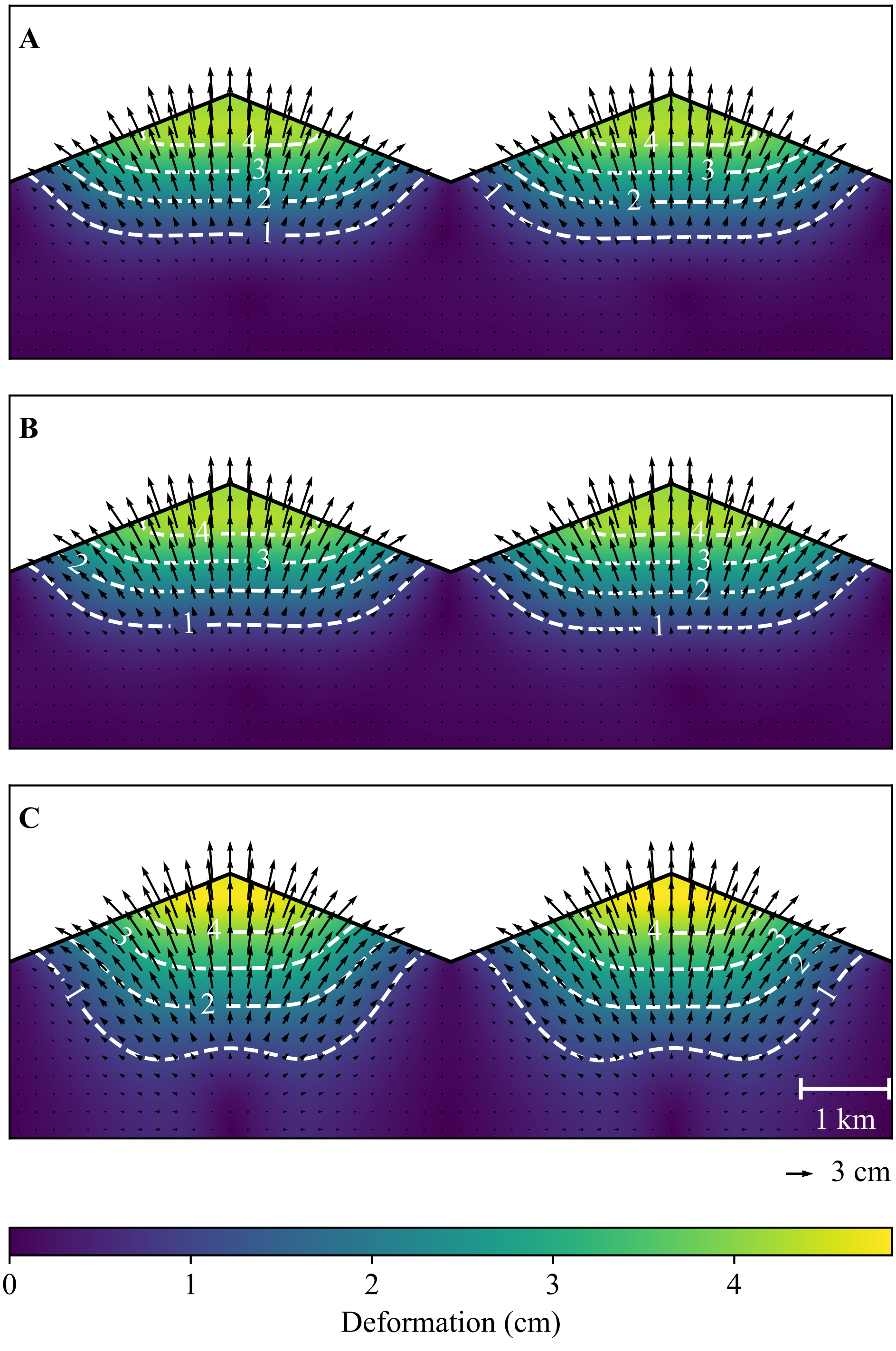

Figure 14. Comparison between recharge-induced deformation for three different models. A: Base case, with random orientation of fractures (Figure 5); B: Set of vertical fractures for mechanical model with imposed pore pressure variations from A; C: Fully coupled hydromechanical model with set of vertical fractures (Figure A1). Colors and contours are deformation magnitudes, arrows also show the deformation directions.

and observed displacement of the surface, together with the anisotropic elasticity. To test which of the two mechanisms described above is dominant, we run the model with a set of vertical fractures (shown in Figure A1), but imposing the exact same pore pressure variations as in the base case (shown in Figure 5). Figure 14A shows the deformation during recharge for the model with random fracture orientation and can be compared with the deformation for the model with vertical fractures (Figure 14B). The difference in deformation is less than a millimeter, while there is a significant increase in deformation (up to 0.8 cm) for the fully coupled hydromechanical model with a set of vertical fractures in Figure 14C. The effect of the anisotropic rock mass permeability is a larger deformation below the crest of the mountains (where recharge occurs) and at depth, and a slightly smaller deformation in the lower half of the slope (see Figure 14). Our model suggests that the primary impact of the preferential fracture orientation on the valley-scale deformation is the redistribution of groundwater flow patterns in the subsurface and not the anisotropic elasticity of the rock mass alone.

The impact of fracture normal stiffness - even when varied in a broad range - on horizontal and vertical displacements is relatively minor and smaller than that of fracture closure and stress ratio. Therefore, we may expect significant coupled recharge-related surface deformations in a wide range of tectonic settings, as long as the rock mass permeability lies in the critical range (approximately $1 \times 10^{-16}\,\mathrm{m}^2$ to $1 \times 10^{-14}\,\mathrm{m}^2$), typical for shallow fractured crystalline rocks in Alpine settings.

6.2 Interpretation of Field Observations at Aletsch

The results of our model scenario dominated by vertical fractures exhibit a similar order of magnitude of ground surface displacement (1 cm to 3 cm) than the ones observed in the Aletsch valley (see Figure 1). Most of the cGPS stations are situated close to the valley bottom or the current position of the glacier margin, and the orientation of the displacement during the snowmelt recharge in spring is subhorizontal. In our model, subhorizontal displacements are also observed for points situated low in the slope in conditions where the hydraulic response zone is strongly controlled by the depth. The station FIES instead is higher in the slope and is displaced at a higher plunge angle during the recharge periods (see Figure 1 and Figure 2), following our model predictions (see Figure A1D). It could indicate a deeper groundwater table below FIES, with a larger vertical pressure-change gradient and hence significant vertical displacement components at the ground surface. Spring line mapping in the area of the crest South-West of FIES (Figure 1) confirms the deep elevation of the groundwater table and the importance of local recharge (Alpiger, 2013).

The station ALTD exhibits very small annual cyclic displacements, suggesting a different hydromechanical situation than that at the other cGPS stations in the valley. According to our model, small ground surface displacement happens in conditions when the pore pressure variations at depth are small, for example, with a very low permeability and a groundwater table very close to the surface (see Figure 11). ALTD is situated behind the head scarp of the Driest instability (Glueer et al., 2021), on stable gneissic bedrock. In the upper slope above ALTD, the Drietsch glacier is providing water to a surface stream (Drieschtbach), which could limit the groundwater table fluctuations in the bedrock slope nearby by contributing to its recharge. In this case, the reduced pore pressure changes during snowmelt at this location could explain the absence of cyclic displacement of the station.

The observations of annual hysteresis in the cGPS stations' position correspond to the ones described in our modeling work during the diffusion of the pore pressure in the hydraulic response zone following the recharge from the snowmelt. All stations have a relatively constant position during winter (November to March, see Figure 2). Then, the stations move out of the slope during the recharge from snowmelt with a plunge angle corresponding to the station's height in the slope, similarly to what is shown in Figure 5D. During the recession, cGPS stations move back to their winter position. At the start, they tend to move horizontally and then vertically in the later stage, inducing the counter-clockwise hysteresis of Figure 2. Such a hysteresis is expected for a pore pressure plume migrating to depth in the slope, as shown in Figure 7 and 8.

Our model results explain many of our detailed field observations in the Aletsch valley, Switzerland, where 6 cGPS stations monitored the ground surface displacement over 7 years. One important feature that is not included in our simulations is the presence of a large glacier in the valley bottom, whose dynamics could also influence the slope's behavior. As shown in Figure 1, the glacier in our study area only covers very small parts of the lowest slope sectors. In addition, as shown by Hugentobler et al. (2022), the superposition of the englacial water pressure fluctuations and the annual slope pressures corresponds to a minor signal at the glacier-slope interface. We found that the magnitude and orientation of ground deformation during a recharge event are consistent with an important hydraulic response zone in the midst of the mountain for the current elevation of the glacier. A station closer to the ridge exhibits a higher plunge of the deformation angle, consistent with a deeper and flatter groundwater table at this location than at other stations. Finally, one station does not exhibit significant annual cyclic displacement, indicating a relatively shallow and stable groundwater table caused by local glacier meltwater recharge in summer.

In our modeling work, we showed that hydraulically active fractures and the variable distribution of their apertures dependent on local stress conditions have a strong impact on the groundwater flow and ground surface deformation. However, previous studies showed that larger transmissive fault zones may also exert a strong impact on the groundwater-related slope deformation, e.g., in the Aletsch valley (Oestreicher et al., 2021). The analysis of the impact of fault zones and their architecture in a fractured bedrock valley is beyond the scope of this paper and is matter of ongoing research. Fault zones, with their much larger scale than typical fractures described above, can significantly modify the nearby hydraulic and mechanical conditions. We expect that some fault zones contain a densely fractured zone and may act as conduit, allowing fast and channelized pressure diffusion at depth. Such channelized effect along discrete features will introduce singular deformation patterns that will depend on fault orientation with respect to slope and the contrast in hydraulic and mechanical properties with the surrounding host rock. The impact of large-scale fault-zones, together with realistic fracture networks, such as those presented in this paper should be investigated in future studies.

7 Conclusions

In this paper, we studied the role of fracture systems in the groundwater-driven deformation of an alpine valley. We showed that the heterogeneity of the fracture density and the anisotropy of the fracture orientation significantly influence the groundwater flow and deformation pattern in valley slopes. Fractures influence the ground deformations in the valley mostly because their influence on the rock mass permeability structure and groundwater flow modifies the region of the slopes that deforms, called the hydraulic response zone in this paper. For a typical slope with a kilometric height and a fluvial v-shape, and typical fractured crystalline rock mass properties, the hydraulic response zone is situated in the midst of the mountain, below the crest, and extends downwards to a depth of a few hundred meters. We observed that the ground surface deformation magnitude and orientation varies through time during and after a recharge event, following the diffusion of the pore pressure front in the slope. The model results allow the interpretation of field observations in the Aletsch valley, Switzerland.

Our findings bring many new insights into understanding groundwater flow and related slope deformations in mountainous environments. Further studies could include applying our model to detailed and realistic alpine valley profiles, including fault zones, and the extension of the model in 3D. Finally, we suggest that the surface deformations also inform on the permeability structure and pore pressure fluctuations at depth, precious information for understanding groundwater flow in fractured bedrock alpine mountain slopes.

Acknowledgments

This project is funded by the Swiss National Science Foundation (project 172492). Q. L. is grateful for the support by the Swiss National Science Foundation (grant number 189882) and the National Natural Science Foundation of China (grant number 41961134032). The displacement data and lineaments used in this study are available through the ETH Research Collections respectively: `https://doi.org/10.3929/ethz-b-000563187` and `https://doi.org/10.3929/ethz-b-000563195`, last accessed in August 2022 and open access upon acceptance of the manuscript for publication. We thank Nadir Dazzi for the help tracing lineaments and during fieldwork, Franziska Glueer and Reto Seifert for installing most of the monitoring system, and Philippe Limpach for the processing of the GNSS data. We thank the many field helpers who gave some time for this project through the years. There would not be enough space here to name them all. We thank Bernadette "Berni" Würsch and Corinne Bischof, Jasmin Maissen, as well as colleagues and friends for their support and all the great discussions.

References

Achtziger-Zupančič, P., Loew, S., & Mariéthoz, G. (2017). A new global database to improve predictions of permeability distribution in crystalline rocks at site scale. *Journal of Geophysical Research: Solid Earth*, *122*(5), 3513–3539. Retrieved from `http://doi.wiley.com/10.1002/2017JB014106` doi: 10.1002/2017JB014106

Alpiger, A. (2013). *Hydrogeology of the Great Aletsch glacier region* (Unpublished doctoral dissertation). ETH Zurich.

Bandis, S. C., Lumsden, A. C., & Barton, N. R. (1983). Fundamentals of rock joint deformation. *International Journal of Rock Mechanics and Mining Sciences & Geomechanics Abstracts*, *20*(6), 249–268. Retrieved from http://www.sciencedirect.com/science/article/pii/0148906283905958 doi: https://doi.org/10.1016/0148-9062(83)90595-8

Banks, D., & Robins, N. (2002). *An introduction to Groundwater in Crystalline Bedrock* (R. Dahl, Ed.). Trondheim, Norway: Norges geologiske undersøkelse (Geological Survey of Norway). Retrieved from http://citeseerx.ist.psu.edu/viewdoc/download?doi=10.1.1.516.8904&rep=rep1&type=pdf

Barton, N. (2013). Shear strength criteria for rock, rock joints, rockfill and rock masses: Problems and some solutions. *Journal of Rock Mechanics and Geotechnical Engineering*, *5*(4), 249–261. Retrieved from https://www.sciencedirect.com/science/article/pii/S1674775513000449https://linkinghub.elsevier.com/retrieve/pii/S1674775513000449 doi: 10.1016/j.jrmge.2013.05.008

Barton, N., Bandis, S., & Bakhtar, K. (1985). Strength, deformation and conductivity coupling of rock joints. *International Journal of Rock Mechanics and Mining Sciences & Geomechanics Abstracts*, *22*(3), 121–140. Retrieved from http://www.sciencedirect.com/science/article/pii/0148906285932279 doi: https://doi.org/10.1016/0148-9062(85)93227-9

Biot, M. A. (1941). General Theory of Three-Dimensional Consolidation. *Journal of Applied Physics*, *12*(2), 155–164. Retrieved from http://aip.scitation.org/doi/10.1063/1.1712886 doi: 10.1063/1.1712886

Bonnet, E., Bour, O., Odling, N. E., Davy, P., Main, I., Cowie, P., & Berkowitz, B. (2001). Scaling of fracture systems in geological media. *Reviews of Geophysics*, *39*(3), 347–383. doi: 10.1029/1999RG000074

Carlsson, H., Carlsson, L., Jamtlid, A., Nordlander, H., Olsson, O., & Olsson, T. (1983). Cross-hole techniques in a deep seated rock mass. *Bulletin of the International Association of Engineering Geology*, *26-27*(1), 377–384. Retrieved from http://link.springer.com/10.1007/BF02594245 doi: 10.1007/BF02594245

Chui, T. F. M., & Freyberg, D. L. (2009). Implementing hydrologic boundary conditions in a multiphysics model. *Journal of Hydrologic Engineering*, *14*(12), 1374–1377. doi: 10.1061/(ASCE)HE.1943-5584.0000113

Dutler, N., Valley, B., Gischig, V., Jalali, M., Brixel, B., Krietsch, H., ... Amann, F. (2020). Hydromechanical insight of fracture opening and closure during in-situ hydraulic fracturing in crystalline rock. *International Journal of Rock Mechanics and Mining Sciences*, *135*(July). doi: 10.1016/j.ijrmms.2020.104450

Eberhardt, E., Preisig, G., & Gischig, V. (2016). Progressive failure in deep-seated rockslides due to seasonal fluctuations in pore pressures and rock mass fatigue. In S. Aversa, L. Cascini, L. Picarelli, & C. Scavia (Eds.), *Landslides and engineered slopes. experience, theory and practice* (Proceeding ed., p. 16). London: CRC Press.

Eberhardt, E., Stead, D., & Coggan, J. (2004). Numerical analysis of initiation and progressive failure in natural rock slopes—the 1991 Randa rockslide. *International Journal of Rock Mechanics and Mining Sciences*, *41*(1), 69–87. Retrieved from `https://linkinghub.elsevier.com/retrieve/pii/S1365160903000765` doi: 10.1016/S1365-1609(03)00076-5

Einstein, H. H., Veneziano, D., Baecher, G. B., & O'Reilly, K. J. (1983). The effect of discontinuity persistence on rock slope stability. *International Journal of Rock Mechanics and Mining Sciences and*, *20*(5), 227–236. doi: 10.1016/0148-9062(83)90003-7

Fu, Y., Dong, Y., Wang, L., Bour, O., Klepikova, M. V., Zong, Z., ... Zhou, Z. (2022). Characteristics of hydraulic conductivity in mountain block systems and its effects on mountain block recharge: Insights from field investigation and numerical modeling. *Journal of Hydrology*, *612*. Retrieved from `https://doi.org/10.1016/j.jhydrol.2022.128184https://linkinghub.elsevier.com/retrieve/pii/S0022169422007570` doi: 10.1016/j.jhydrol.2022.128184

Gan, Q., & Elsworth, D. (2016). A continuum model for coupled stress and fluid flow in discrete fracture networks. *Geomechanics and Geophysics for Geo-Energy and Geo-Resources*, *2*(1), 43–61. doi: 10.1007/s40948-015-0020-0

Gleeson, T., & Manning, A. H. (2008). Regional groundwater flow in mountainous terrain: Three-dimensional simulations of topographic and hydrogeologic controls. *Water Resources Research*, *44*(10). Retrieved from https://agupubs.onlinelibrary.wiley.com/doi/abs/10.1029/2008WR006848http://doi.wiley.com/10.1029/2008WR006848 doi: 10.1029/2008WR006848

Glueer, F., Loew, S., Seifert, R., Aaron, J., Grämiger, L., Conzett, S., … Manconi, A. (2021). Robotic Total Station Monitoring in High Alpine Paraglacial Environments: Challenges and Solutions from the Great Aletsch Region (Valais, Switzerland). *Geosciences*, *11*(11), 471. Retrieved from https://www.mdpi.com/2076-3263/11/11/471 doi: 10.3390/geosciences11110471

Goderniaux, P., Davy, P., Bresciani, E., de Dreuzy, J.-R., & Le Borgne, T. (2013). Partitioning a regional groundwater flow system into shallow local and deep regional flow compartments. *Water Resources Research*, *49*(4), 2274–2286. Retrieved from https://agupubs.onlinelibrary.wiley.com/doi/abs/10.1002/wrcr.20186 doi: 10.1002/wrcr.20186

Grämiger, L. M., Moore, J. R., Gischig, V. S., Ivy-Ochs, S., & Loew, S. (2017). Beyond debuttressing: Mechanics of paraglacial rock slope damage during repeat glacial cycles. *Journal of Geophysical Research: Earth Surface*, *122*(4), 1004–1036. Retrieved from http://doi.wiley.com/10.1002/2016JF003967 doi: 10.1002/2016JF003967

Grämiger, L. M., Moore, J. R., Gischig, V. S., Loew, S., Funk, M., & Limpach, P. (2020). Hydromechanical Rock Slope Damage During Late Pleistocene and Holocene Glacial Cycles in an Alpine Valley. *Journal of Geophysical Research: Earth Surface*, *125*(8), 1–24. Retrieved from https://onlinelibrary.wiley.com/doi/10.1029/2019JF005494 doi: 10.1029/2019JF005494

Hansmann, J., Loew, S., & Evans, K. F. (2012). Reversible rock-slope deformations caused by cyclic water-table fluctuations in mountain slopes of the Central Alps, Switzerland. *Hydrogeology Journal*, *20*(1), 73–91. Retrieved from http://link.springer.com/10.1007/s10040-011-0801-7 doi: 10.1007/s10040-011-0801-7

Hoek, E., & Brown, E. T. (1997). Practical estimates of rock mass strength. *International Journal of Rock Mechanics and Mining Sciences*, *34*(8), 1165–1186. doi: 10.1016/S1365-1609(97)80069-X

Hoek, E., & Diederichs, M. S. (2006). Empirical estimation of rock mass modulus. *International Journal of Rock Mechanics and Mining Sciences*, *43*(2), 203–215. doi: 10.1016/j.ijrmms.2005.06.005

Hugentobler, M., Aaron, J., Loew, S., & Roques, C. (2022). Hydro-Mechanical Interactions of a Rock Slope With a Retreating Temperate Valley Glacier. *Journal of Geophysical Research: Earth Surface*, *127*(4). Retrieved from `https://onlinelibrary.wiley.com/doi/10.1029/2021JF006484` doi: 10.1029/2021JF006484

Jaeger, J. C., Cook, N. G. W., & Zimmerman, R. W. (2007). *Fundamentals of rock mechanics - Fourth edition* (4th editio ed.). Oxford: Wiley-Blackwell. doi: 10.1016/0040-1951(77)90223-2

Ladanyi, B., & Archambault, G. (1969). *Simulation Of Shear Behavior Of A Jointed Rock Mass.*

Lei, Q., & Barton, N. (2022). On the selection of joint constitutive models for geomechanics simulation of fractured rocks. *Computers and Geotechnics*, *145*(February), 104707. Retrieved from `https://doi.org/10.1016/j.compgeo.2022.104707` doi: 10.1016/j.compgeo.2022.104707

Lei, Q., & Gao, K. (2018). Correlation Between Fracture Network Properties and Stress Variability in Geological Media. *Geophysical Research Letters*, *45*(9), 3994–4006. doi: 10.1002/2018GL077548

Lei, Q., Gholizadeh Doonechaly, N., & Tsang, C.-F. (2021). Modelling fluid injection-induced fracture activation, damage growth, seismicity occurrence and connectivity change in naturally fractured rocks. *International Journal of Rock Mechanics and Mining Sciences*, *138*. Retrieved from `https://linkinghub.elsevier.com/retrieve/pii/S1365160920309643` doi: 10.1016/j.ijrmms.2020.104598

Lei, Q., Latham, J.-P., & Tsang, C.-F. (2017). The use of discrete fracture networks for modelling coupled geomechanical and hydrological behaviour of fractured rocks. *Computers and Geotechnics*, *85*, 151–176. Retrieved from `https://www.sciencedirect.com/science/article/pii/S0266352X16303317` doi: 10.1016/J.COMPGEO.2016.12.024

Lei, Q., Latham, J.-P., & Xiang, J. (2016). Implementation of an Empirical Joint Constitutive Model into Finite-Discrete Element Analysis of the Geomechanical Behaviour of Fractured Rocks. *Rock Mechanics and Rock Engineering*, *49*(12), 4799–4816. Retrieved from http://link.springer.com/10.1007/s00603-016-1064-3 doi: 10.1007/s00603-016-1064-3

Lei, Q., Latham, J. P., Xiang, J., & Tsang, C. F. (2015). Polyaxial stress-induced variable aperture model for persistent 3D fracture networks. *Geomechanics for Energy and the Environment*, *1*, 34–47. Retrieved from http://dx.doi.org/10.1016/j.gete.2015.03.003 doi: 10.1016/j.gete.2015.03.003

Lei, Q., & Wang, X. (2016). Tectonic interpretation of the connectivity of a multi-scale fracture system in limestone. *Geophysical Research Letters*, *43*(4), 1551–1558. doi: 10.1002/2015GL067277

Lei, Q., Wang, X., Min, K. B., & Rutqvist, J. (2020). Interactive roles of geometrical distribution and geomechanical deformation of fracture networks in fluid flow through fractured geological media. *Journal of Rock Mechanics and Geotechnical Engineering*, *12*(4), 780–792. Retrieved from https://doi.org/10.1016/j.jrmge.2019.12.014 doi: 10.1016/j.jrmge.2019.12.014

Limpach, P., Geiger, A., & Raetzo, H. (2016). GNSS for Deformation and Geohazard Monitoring in the Swiss Alps. In *Proceedings of the 3rd joint international symposium on deformation monitoring (jisdm 2016), vienna* (pp. 1–4). Vienna.

Liu, H. H., Bodvarsson, G. S., & Finsterle, S. (2002). A note on unsaturated flow in two-dimensional fracture networks. *Water Resources Research*, *38*(9), 15–1. doi: 10.1029/2001wr000977

Loew, S., Ebneter, F., Bremen, R., Herfort, M., Lützenkirchen, V., & Matousek, F. (2007). Annual Opening and Closure of Alpine Valleys. *Felsbau : rock and soil engineering*, *25*(5), 1–60. Retrieved from https://structurae.net/en/literature/journal-article/annual-opening-and-closure-of-alpine-valleys

Loew, S., Lützenkirchen, V., Hansmann, J., Ryf, A., & Guntli, P. (2015). Transient surface deformations caused by the Gotthard Base Tunnel. *International Journal of Rock Mechanics and Mining Sciences*. doi: 10.1016/j.ijrmms.2014.12.009

Manga, M., Beresnev, I., Brodsky, E. E., Elkhoury, J. E., Elsworth, D., Ingebritsen, S. E., ... Wang, C. Y. (2012). Changes in permeability caused by transient stresses: Field observations, experiments, and mechanisms. *Reviews of Geophysics*, *50*(2). doi: 10.1029/2011RG000382

Manning, C. E., & Ingebritsen, S. E. (1999). Permeability of the continental crust: Implications of geothermal data and metamorphic systems. *Reviews of Geophysics*, *37*(1), 127–150. doi: 10.1029/1998RG900002

Markovich, K. H., Manning, A. H., Condon, L. E., & McIntosh, J. C. (2019). Mountain-block Recharge: A Review of Current Understanding. *Water Resources Research*, 2019WR025676. Retrieved from `https://onlinelibrary.wiley.com/doi/abs/10.1029/2019WR025676` doi: 10.1029/2019WR025676

Min, K.-B., Rutqvist, J., Tsang, C.-F., & Jing, L. (2004). Stress-dependent permeability of fractured rock masses: a numerical study. *International Journal of Rock Mechanics and Mining Sciences*, *41*(7), 1191–1210. Retrieved from `https://linkinghub.elsevier.com/retrieve/pii/S1365160904002473` doi: 10.1016/j.ijrmms.2004.05.005

Moon, S., Perron, J. T., Martel, S. J., Goodfellow, B. W., Mas Ivars, D., Hall, A., … Stroeven, A. P. (2020). Present-Day Stress Field Influences Bedrock Fracture Openness Deep Into the Subsurface. *Geophysical Research Letters*, *47*(23). Retrieved from `https://onlinelibrary.wiley.com/doi/10.1029/2020GL090581` doi: 10.1029/2020GL090581

Noorian Bidgoli, M., & Jing, L. (2014). Anisotropy of strength and deformability of fractured rocks. *Journal of Rock Mechanics and Geotechnical Engineering*, *6*(2), 156–164. Retrieved from `http://dx.doi.org/10.1016/j.jrmge.2014.01.009` doi: 10.1016/j.jrmge.2014.01.009

Oda, M. (1986). An equivalent continuum model for coupled stress and fluid flow analysis in jointed rock masses. *Water Resources Research*, *22*(13), 1845–1856. doi: 10.1029/WR022I013P01845

Oda, M., Yamabe, T., Ishizuka, Y., Kumasaka, H., Tada, H., & Kimura, K. (1993). Elastic stress and strain in jointed rock masses by means of crack tensor analysis. *Rock Mechanics and Rock Engineering*, *26*(2), 89–112. Retrieved from `http://link.springer.com/10.1007/BF01023618` doi: 10.1007/BF01023618

Oestreicher, N., Loew, S., Roques, C., Aaron, J., Gualandi, A., Longuevergne, L., … Hugentobler, M. (2021). Controls on Spatial and Temporal Patterns of Slope

Deformation in an Alpine Valley. *Journal of Geophysical Research: Earth Surface*, *126*(12). doi: 10.1029/2021jf006353

Ofterdinger, U. S., Renard, P., & Loew, S. (2014). Hydraulic subsurface measurements and hydrodynamic modelling as indicators for groundwater flow systems in the Rotondo granite, Central Alps (Switzerland). *Hydrological Processes*, *28*(2), 255–278. Retrieved from `http://doi.wiley.com/10.1002/hyp.9568` doi: 10.1002/hyp.9568

Pintori, F., Serpelloni, E., Longuevergne, L., Garcia, A., Faenza, L., D'Alberto, L., ... Belardinelli, M. E. (2021). Mechanical Response of Shallow Crust to Groundwater Storage Variations: Inferences from Deformation and Seismic Observations in the Eastern Southern Alps, Italy. *Journal of Geophysical Research: Solid Earth*, 2020JB020586. Retrieved from `https://onlinelibrary.wiley.com/doi/10.1029/2020JB020586` doi: 10.1029/2020JB020586

Preisig, G., Cornaton, F. J., & Perrochet, P. (2012). Simulation of flow in fractured rocks using effective stress-dependent parameters and aquifer consolidation. In *Proceedings of the {modelcare}* (pp. 273–279). Retrieved from `http://doc.rero.ch/record/31578`

Pruess, K. (1999). A mechanistic model for water seepage through thick unsaturated zones in fractured rocks of low matrix permeability. *Water Resources Research*, *35*(4), 1039–1051. doi: 10.1029/1998WR900100

Rahman, M. K., Hossain, M. M., & Rahman, S. S. (2002). A shear-dilation-based model for evaluation of hydraulically stimulated naturally fractured reservoirs. *International Journal for Numerical and Analytical Methods in Geomechanics*, *26*(5), 469–497. doi: 10.1002/nag.208

Rapp, G. A., Condon, L. E., & Markovich, K. H. (2020). Sensitivity of Simulated Mountain Block Hydrology to Subsurface Conceptualization. *Water Resources Research*, *56*(10). doi: 10.1029/2020WR027714

Ren, F., Ma, G., Fu, G., & Zhang, K. (2015). Investigation of the permeability anisotropy of 2D fractured rock masses. *Engineering Geology*, *196*, 171–182. Retrieved from `http://dx.doi.org/10.1016/j.enggeo.2015.07.021` doi: 10.1016/j.enggeo.2015.07.021

Rouyet, L., Kristensen, L., Derron, M.-H., Michoud, C., Blikra, L. H., Jaboyedoff, M., & Lauknes, T. R. (2017). Evidence of rock slope breathing using ground-based InSAR. *Geomorphology*, *289*, 152–169. Retrieved from http://linkinghub.elsevier.com/retrieve/pii/S0169555X16305505https://linkinghub.elsevier.com/retrieve/pii/S0169555X16305505 doi: 10.1016/j.geomorph.2016.07.005

Rutqvist, J., Leung, C., Hoch, A., Wang, Y., & Wang, Z. (2013). Linked multicontinuum and crack tensor approach for modeling of coupled geomechanics, fluid flow and transport in fractured rock. *Journal of Rock Mechanics and Geotechnical Engineering*, *5*(1), 18–31. Retrieved from https://linkinghub.elsevier.com/retrieve/pii/S1674775513000073 doi: 10.1016/j.jrmge.2012.08.001

Rutqvist, J., & Stephansson, O. (2003). The role of hydromechanical coupling in fractured rock engineering. *Hydrogeology Journal*, *11*(1), 7–40. Retrieved from http://link.springer.com/10.1007/s10040-002-0241-5 doi: 10.1007/s10040-002-0241-5

Salimzadeh, S., Paluszny, A., Nick, H. M., & Zimmerman, R. W. (2018). Geothermics A three-dimensional coupled thermo-hydro-mechanical model for deformable fractured geothermal systems. *Geothermics*, *71*, 212–224. Retrieved from http://dx.doi.org/10.1016/j.geothermics.2017.09.012 doi: 10.1016/j.geothermics.2017.09.012

Sánchez, L., Völksen, C., Sokolov, A., Arenz, H., & Seitz, F. (2018). Present-day surface deformation of the Alpine region inferred from geodetic techniques. *Earth System Science Data*, *10*(3), 1503–1526. doi: 10.5194/essd-10-1503-2018

Serpelloni, E., Pintori, F., Gualandi, A., Scoccimarro, E., Cavaliere, A., Anderlini, L., … Todesco, M. (2018). Hydrologically Induced Karst Deformation: Insights From GPS Measurements in the Adria-Eurasia Plate Boundary Zone. *Journal of Geophysical Research: Solid Earth*. doi: 10.1002/2017JB015252

Silverii, F., Montgomery-Brown, E. K., Borsa, A. A., & Barbour, A. J. (2020). Hydrologically Induced Deformation in Long Valley Caldera and Adjacent Sierra Nevada. *Journal of Geophysical Research: Solid Earth*, *125*(5). Retrieved from https://onlinelibrary.wiley.com/doi/abs/10.1029/2020JB019495 doi: 10.1029/2020JB019495

Steck, A. (2022). *Geological Vector Atlas Aletschgletscher (LK 1269), map sheet 131, V2* (Vol. V2). Wabern: Federal Office of Topography swisstopo.

Sternai, P., Sue, C., Husson, L., Serpelloni, E., Becker, T. W., Willett, S. D., ... Castelltort, S. (2019). Present-day uplift of the European Alps: Evaluating mechanisms and models of their relative contributions. *Earth-Science Reviews*, *190*, 589–604. Retrieved from https://www.sciencedirect.com/science/article/pii/S0012825218304136#f0025https://linkinghub.elsevier.com/retrieve/pii/S0012825218304136 doi: 10.1016/j.earscirev.2019.01.005

Terzaghi, K. (1923). Die Berechnung der Durchlässigkeitsziffer des Tones aus dem Verlauf der hydrodynamischen Spannungserscheinungen. *Sitzungsberichte der Akademie der Wissenschaften in Wien, Mathematisch-Naturwissenschaftliche Klasse, Abteilung IIa*(132), 125–138.

Tsang, C. F., Barnichon, J. D., Birkholzer, J., Li, X. L., Liu, H. H., & Sillen, X. (2012). Coupled thermo-hydro-mechanical processes in the near field of a high-level radioactive waste repository in clay formations. *International Journal of Rock Mechanics and Mining Sciences*, *49*, 31–44. doi: 10.1016/j.ijrmms.2011.09.015

Tsang, C. F., Rutqvist, J., & Min, K. B. (2007). Fractured rock hydromechanics: From borehole testing to solute transport and CO2 storage. *Geological Society Special Publication*, *284*(3), 15–34. doi: 10.1144/SP284.2

Ucar, E., Berre, I., & Keilegavlen, E. (2017). Postinjection Normal Closure of Fractures as a Mechanism for Induced Seismicity. *Geophysical Research Letters*, *44*(19), 9598–9606. doi: 10.1002/2017GL074282

Wang, H. F. (2000). *Theory of linear poroelasticity with applications to geomechanics and hydrogeology.* Princeton University Press. Retrieved from https://press.princeton.edu/titles/7006.html

Wang, L., & Lei, Q. (2021). A dual-scale fracture network model for computing hydro-mechanical properties of fractured rock. *Computers and Geotechnics*, *138*. Retrieved from https://linkinghub.elsevier.com/retrieve/pii/S0266352X21003542 doi: 10.1016/j.compgeo.2021.104357

Welch, L. A., & Allen, D. M. (2012). Consistency of groundwater flow patterns in mountainous topography: Implications for valley bottom water replenishment and for defining groundwater flow boundaries. *Water Resources Research*, *48*(5). Retrieved from http://dx.doi.org/10.1029/2011WR010901http://doi.wiley.com/10.1029/2011WR010901 doi: 10.1029/2011WR010901

Welch, L. A., & Allen, D. M. (2014). Hydraulic conductivity characteristics in mountains and implications for conceptualizing bedrock groundwater flow. *Hydrogeology Journal*, *22*(5), 1003–1026. Retrieved from http://link.springer.com/10.1007/s10040-014-1121-5 doi: 10.1007/s10040-014-1121-5

Willis-Richards, J., Watanabe, K., & Takahashi, H. (1996). Progress toward a stochastic rock mechanics model of engineered geothermal systems. *Journal of Geophysical Research: Solid Earth*, *101*(B8), 17481–17496. Retrieved from http://doi.wiley.com/10.1029/96JB00882 doi: 10.1029/96JB00882

Witherspoon, P. A., Wang, J. S. Y., Iwai, K., & Gale, J. E. (1980). Validity of Cubic Law for fluid flow in a deformable rock fracture. *Water Resources Research*, *16*(6), 1016–1024. Retrieved from http://doi.wiley.com/10.1029/WR016i006p01016 doi: 10.1029/WR016i006p01016

Zhao, C., Zhang, Z., & Lei, Q. (2021). Role of hydro-mechanical coupling in excavation-induced damage propagation, fracture deformation and microseismicity evolution in naturally fractured rocks. *Engineering Geology*, *289*, 106169. Retrieved from https://doi.org/10.1016/j.enggeo.2021.106169 doi: 10.1016/j.enggeo.2021.106169

Zimmerman, R., & Main, I. (2004). Hydromechanical Behavior of Fractured Rocks. In Y. Guéguen & M. Boutéca (Eds.), *Mechanics of fluid-saturated rocks* (Vol. 89, pp. 363–421). Academic Press. Retrieved from http://www.sciencedirect.com/science/article/pii/S0074614203800232 doi: https://doi.org/10.1016/S0074-6142(03)80023-2

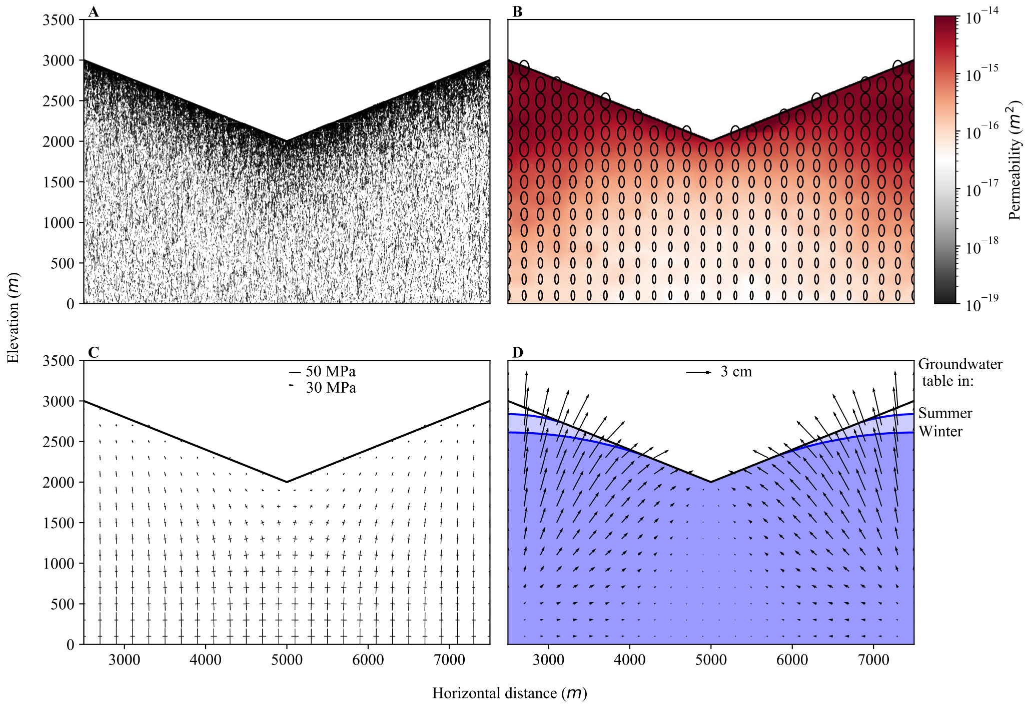

Figure A1. Model with one set of vertical fractures. **A:** Generated discrete fracture network for a vertical set of fractures. **B:** Permeability field, with permeability ellipses scaled with the logarithm of the permeability magnitude. **C:** Stress modeled in the valley (the length and orientation of each line represent the magnitude and orientation of principal stresses). **D:** Observed change in groundwater table before and after the spring infiltration from snowmelt, and corresponding displacement observed in the rock mass between these two instants.

Appendix A Appendix

A1 Effect of the Orientation of a Single Fracture Set

A2 Effect of Depth-Dependent Fracture Density

A3 Effect of Fracture Stiffness and Maximum Closure

Increasing the initial fracture stiffness decreases the hydraulic gradient (Figure A7A). Here, we fix the ratio between initial fracture normal stiffness and initial fracture shear stiffness at 2. The change in hydraulic gradient during the recharge is 0.124 for an initial normal stiffness of 20 GPa/m and is reduced to 0.095 for an initial normal stiffness of 60 GPa/m. However, the head difference during the recharge period increases with the initial fracture stiffness for points in the lower part of the slope, is relatively stable for

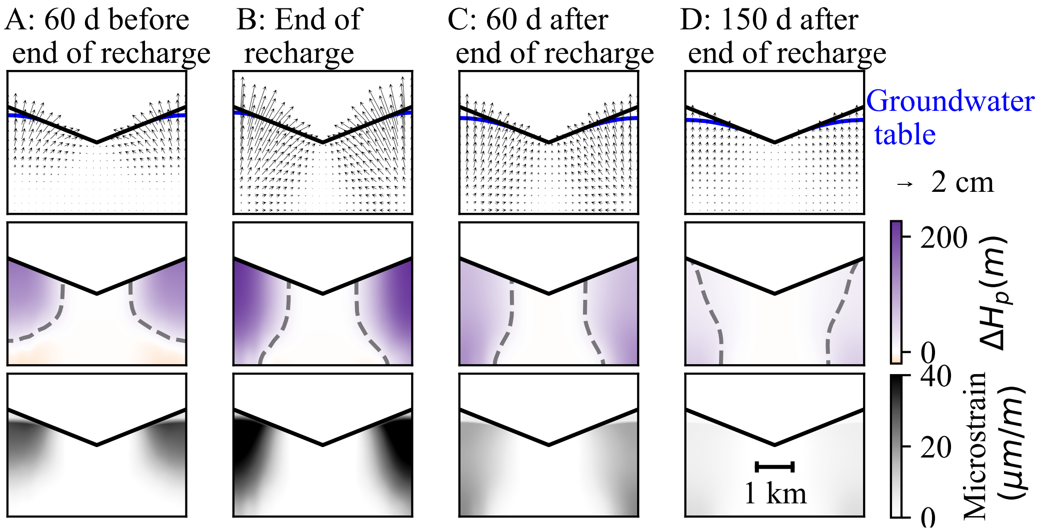

Figure A2. Model with vertical set of fractures and selected times for comparison with low water table conditions before the recharge starts. The first row shows the displacement field relative to the start of the recharge (black arrows, whose length is the magnitude of the deformation) and the groundwater table (continuous blue lines). The second row shows the head pressure difference relative to the low water table conditions. The pore pressure plume is in purple (dashed line is 20 m contour line, delimited to help the reader visualize the propagation of the pore pressure diffusion front). The last row shows the corresponding deformation field in microstrain ($\mu m/m$).

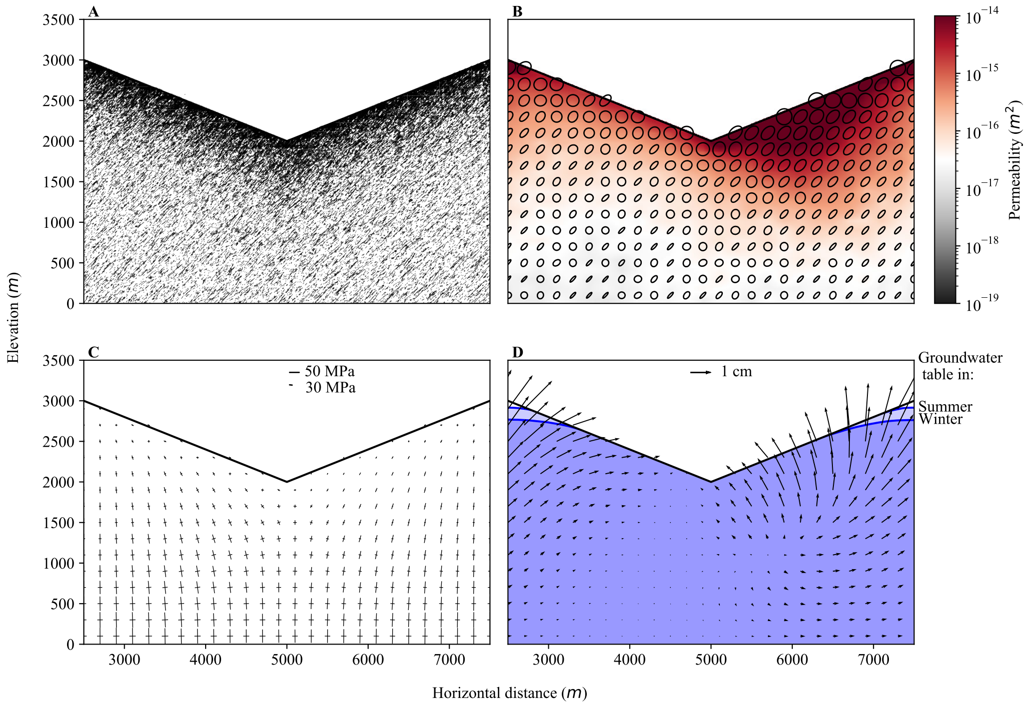

Figure A3. Model with one set of inclined fractures. **A:** Generated discrete fracture network for a 45° inclined set of fractures. **B:** Permeability field, with permeability ellipses scaled with the logarithm of the permeability magnitude. **C:** Stress modeled in the valley (the length and orientation of each line represent the magnitude and orientation of principal stresses). **D:** Observed change in groundwater table before and after the spring infiltration from snowmelt, and corresponding displacement observed in the rock mass between these two instants.

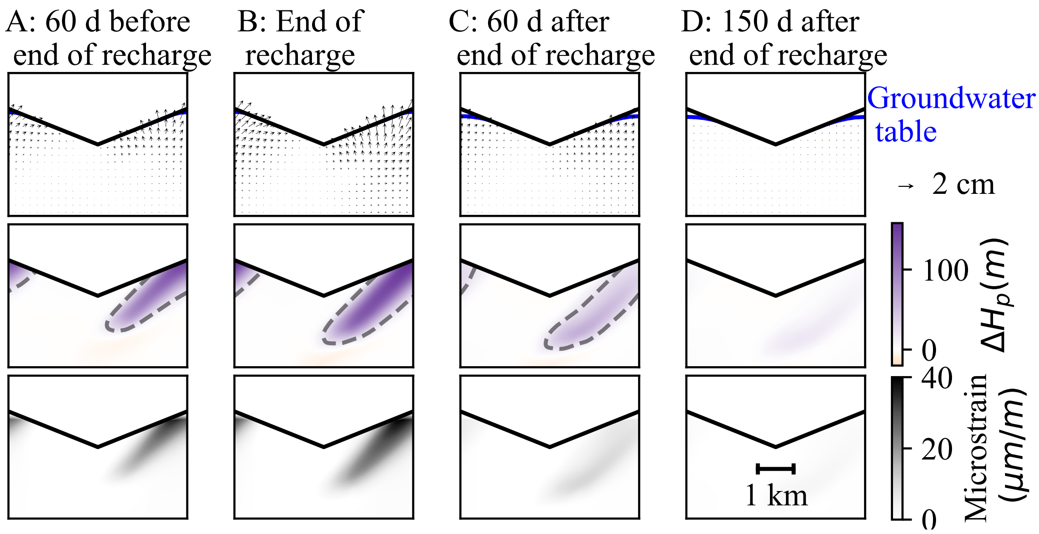

Figure A4. Model with set of oblique fractures and selected times for comparison with low water table conditions before the recharge starts. The first row shows the displacement field relative to the start of the recharge (black arrows, whose length is the magnitude of the deformation) and the groundwater table (continuous blue lines). The second row shows the head pressure difference relative to the low water table conditions. The pore pressure plume is in purple (dashed line is 20 m contour line, delimited to help the reader visualize the propagation of the pore pressure diffusion front). The last row shows the corresponding deformation field in microstrain ($\mu m/m$).

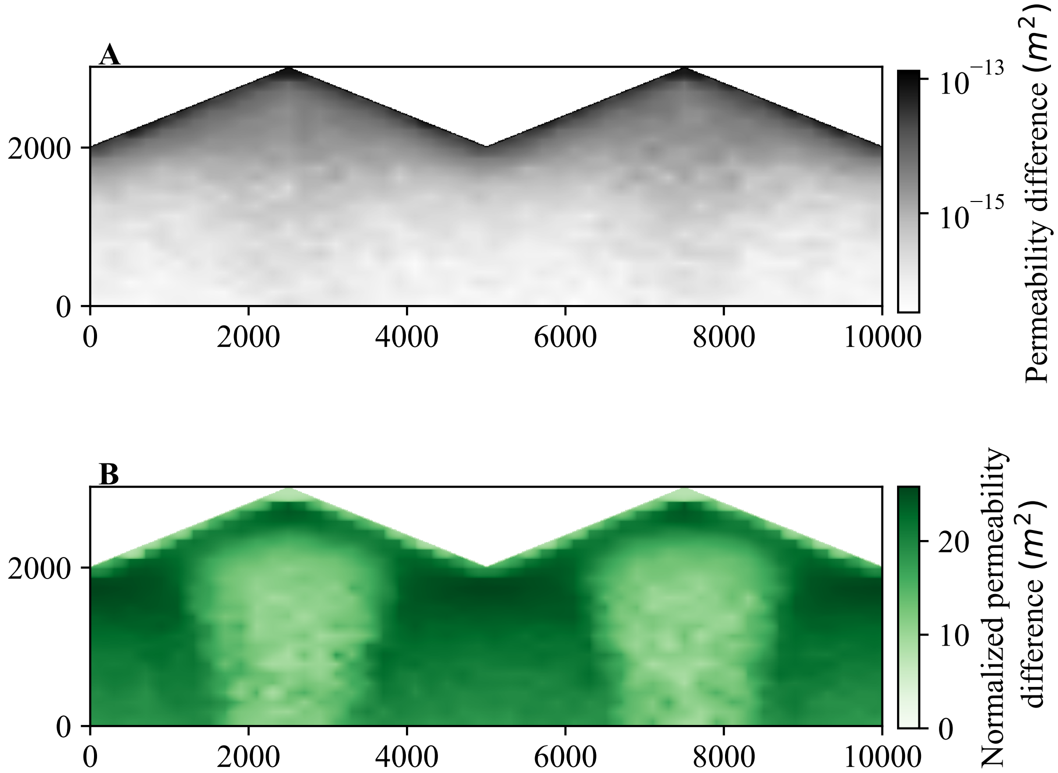

Figure A5. A: Permeability difference between a model with initial fracture aperture fixed at 0.089 mm and 0.183 mm. B: Same permeability change relative to the permeability for an initial fracture aperture fixed at 0.089 mm.

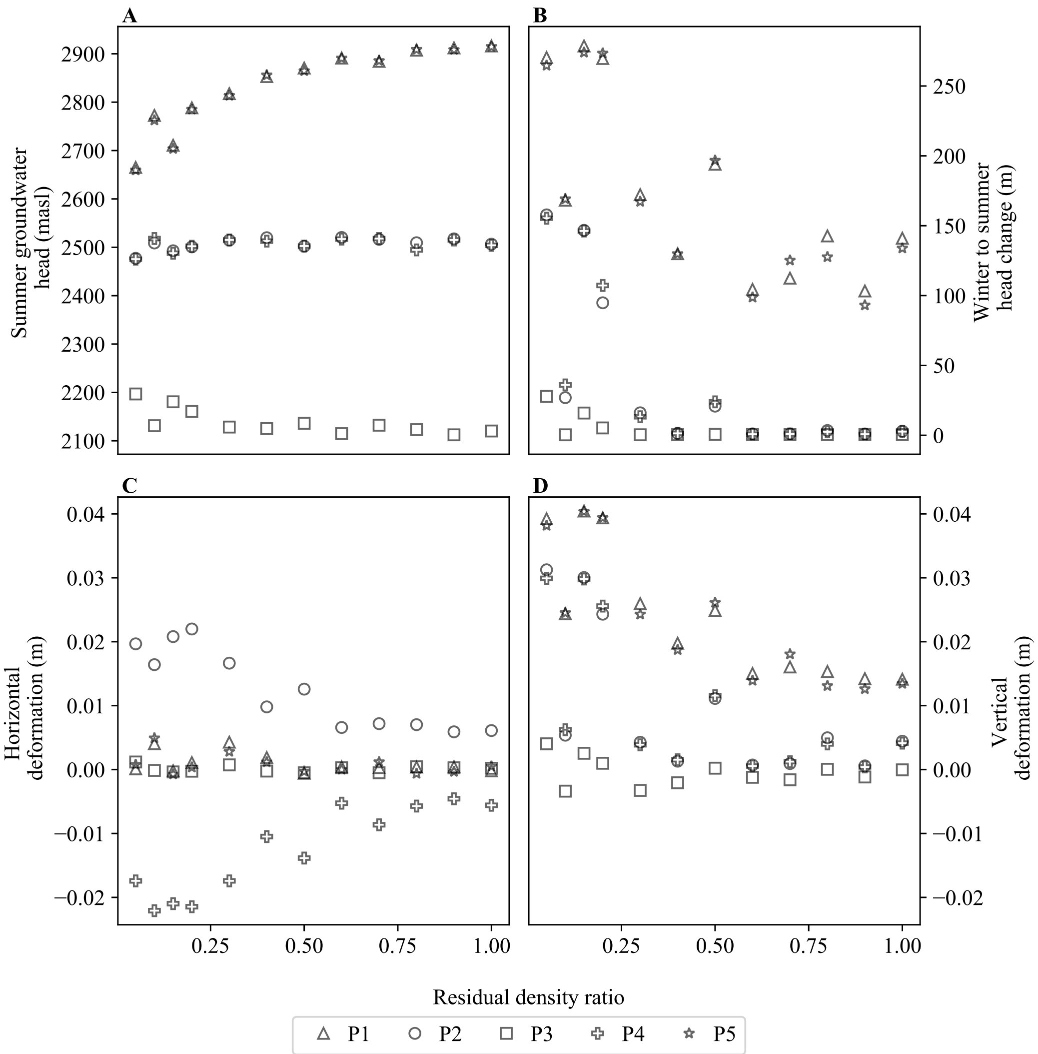

Figure A6. Effect of depth-dependent fracture density on groundwater table fluctuations and deformation at the five control points from Figure 4 between wet and dry conditions. A: Groundwater table elevation in wet conditions; B: Groundwater table elevation changes between dry and wet states; C: Horizontal and D: Vertical deformation between dry and wet states.

points at the mid-slope and decreases for points at the crest (Figure A7B). Similarly, the vertical displacement during the recharge increases with the initial fracture stiffness for points in the lower and mid-slope. It first increases then decreases slightly for points at the crest (Figure A7D). The horizontal displacement is negligible for points in the middle of the valley and at the crests and decreases with the increase of the initial stiffness for points at mid-slope (Figure A7C).

In Figure A8, we vary the maximum fracture closure (i.e., the difference between the initial and residual apertures). The horizontal displacement is negligible at the valley bottom and crests. However, it increases with the maximum allowable closure together with the hydraulic gradient of the groundwater table in the slope (Figure A8A). The vertical displacement generally decreases with the increase of the maximum allowable closure (Figure A8D). We note that decreasing the maximum allowable closure leads to a change in the head during recharge even below the valley (Figure A8B), in which case the entire valley is deforming upwards during recharge (Figure A8D).

A4 Effect of Slope Steepness

The ground surface can play an important role in the pore pressure-driven displacement process because the recharge and seepage take place on this boundary. Furthermore, the topography may also affect the stress and strain distribution, especially in the near-surface region. Modifying the topography in the model could change the infiltration pattern and subsurface properties of the system. We modify the slope angle of the topography by increasing the vertical distance between the mountain crest and valley bottom while keeping exactly the same valley width, fracture density depth-dependency, and precipitation rate. The trend toward larger permeability below the crests than below the valley center (Figure 5 and Figure 6) increases with the height of the slope. The high-permeability zone below the mountain crests extends below the level of the valley bottom (e.g., Figure 5) for all the models. Below the valley, we observe a decrease of the permeability, together with an increase of the stress magnitude, indicative of a decrease in the fracture aperture in this part of the model.

Models with steeper slopes tend to have a deeper unsaturated zone below the crests for the same recharge rate. The displacement observed at the surface exhibits a strong horizontal component at the bottom of the slope, where the groundwater table reaches

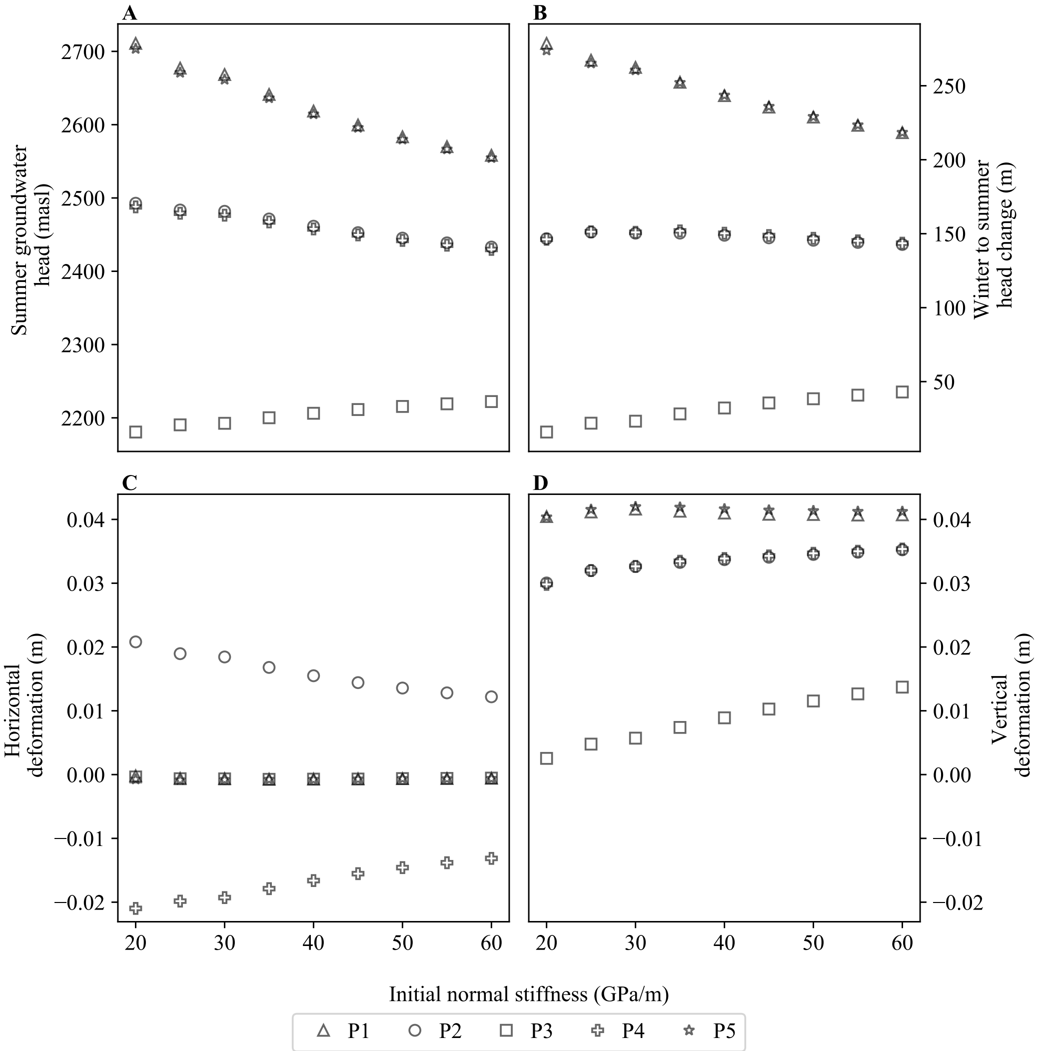

Figure A7. Effect of initial fracture stiffness on groundwater table fluctuations and deformation at the five control points from Figure 4 between wet and dry conditions. The initial shear stiffness is always half the initial normal stiffness. A: Groundwater table elevation in wet conditions; B: Groundwater table elevation changes between dry and wet states; C: Horizontal and D: Vertical deformation between dry and wet states.

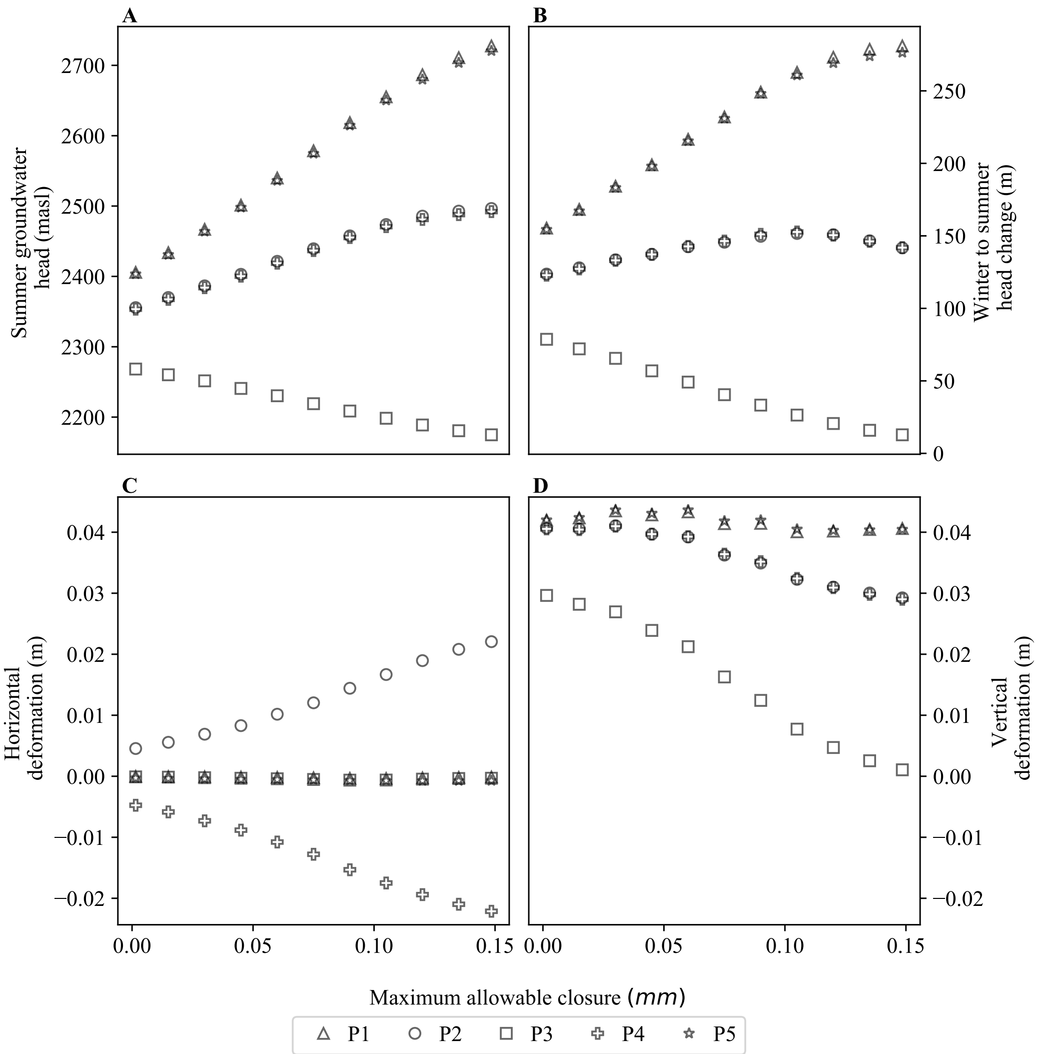

Figure A8. Effect of fracture maximum allowable closure on groundwater table fluctuations and deformation at the five control points from Figure 4 between wet and dry conditions. A: Groundwater table elevation in wet conditions; B: Groundwater table elevation changes between dry and wet states; C: Horizontal and D: Vertical deformation between dry and wet states.

the surface. Higher, the orientation of the displacement rotates towards upward vertical motion with reduced magnitude. Despite the groundwater table variations being relatively similar between the models with different slope steepness (approximately 250 m), the magnitude of the displacement is significantly larger for systems with steeper and higher slopes.